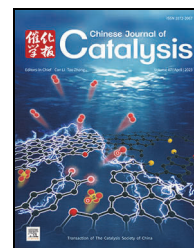


available at www.sciencedirect.comjournal homepage: www.sciencedirect.com/journal/chinese-journal-of-catalysis

Review

Heteronuclear dual-metal atom catalysts for nanocatalytic tumor therapy



Jingyi Han, Jingqi Guan *

Institute of Physical Chemistry, College of Chemistry, Jilin University, Changchun 130021, Jilin, China

ARTICLE INFO

Article history:

Received 30 October 2022

Accepted 1 December 2022

Available online 20 March 2023

Keywords:

Heteronuclear

Dual-atom catalyst

Tumor therapy

Reactive oxygen

Fenton-like reaction

ABSTRACT

Due to excellent catalytic activity and high atomic utilization rate, single atom catalysts (SACs) have become a rising star in the field of nanocatalytic medicine. Heteronuclear dual-atom catalysts (HDACs) retain the advantages of monoatomic catalysts, have more optionally regulated coordination environment, possess favorable synergistic effects between different active sites, and can break through the restriction of adsorption ratio of SACs, making them the most ideal candidates for catalytic tumor therapy. In this review, we first introduce the advanced characterization methods of HDACs. Then, HDACs in different application fields are classified and elaborated according to various preparation strategies. According to the pharmacodynamic mechanisms, the application of HDACs in the field of nanocatalytic tumor therapy is emphatically introduced. Finally, a concise but focused summary and perspective is provided to outline the current challenges and prospects for future development of HDACs for oncology therapy.

© 2023, Dalian Institute of Chemical Physics, Chinese Academy of Sciences.

Published by Elsevier B.V. All rights reserved.

1. Introduction

With the rapid development of medicine and biology, people have a deeper understanding of tumor. However, the latest statistics show that the mortality rate of cancers such as liver and stomach cancers keeps up and the projections for 2050 are still far from optimistic with nearly 100000 people dying of cancer worldwide, making it remain one of the most recognized threats to human health. At present, chemotherapy [1], radiotherapy [2] and surgery [3] are the three traditional strategies of clinical cancer treatment, which have been widely used for decades. Although their treatment technology is mature and effective, they still have inevitable defects. For example, high doses of radiation have the severe side effect of simultaneously destroying healthy tissue. Chemotherapy drugs, including platinum compounds and anticancer antibiotics, usually have

strong resistance and sensitization causing them unable to be widely used. Therefore, the clinical treatment of chemoradiotherapy is usually only applied to patients with advanced stage, they also suffer great pain during the treatment [4]. Conventional surgical treatment mainly involves the direct removal of tumor tissue, while this method is helpless for leukemia and metastatic cancer.

With the development of nanomaterials [5–9], various emerging catalytic anti-tumor materials have been widely studied and reported [10–13]. Their treatment approach is mainly through catalyzing H_2O_2 , H_2O or O_2 to generate a large number of reactive oxygen species (ROS) including superoxide ion ($\text{O}_2^{\cdot-}$), singlet oxygen ($^1\text{O}_2$) and hydroxyl radical ($\cdot\text{OH}$), which can effectively induce the autonomous apoptosis of malignant cells [14–17]. This intratumoral chemistry shows great potential to attenuate side effects. Although great accomplish-

* Corresponding author. E-mail: guanjq@jlu.edu.cn (J. Guan).

This work was supported by the National Natural Science Foundation of China (22075099), the Natural Science Foundation of Jilin Province (20220101051JC), and the Education Department of Jilin Province (JJKH20220967KJ).

[https://doi.org/10.1016/S1872-2067\(22\)64207-4](https://doi.org/10.1016/S1872-2067(22)64207-4)

ment has been achieved in catalytic chemical reaction (CCR) nanomedicine, there are still problems that need to be addressed [18]. For example, although the concentration of H_2O_2 , O_2 and other ROS sources has obvious advantages compared with normal tissues, it still stays in the order of mere $100\ \mu\text{m}$ as limited by the low-pH and hypoxic tumor micro environment (TME). Furthermore, the targeting of tumor tissue is poor, and therapeutic efficiency and drug toxicity need to be further improved and reduced, respectively. Therefore, it is still an urgent need to develop new anti-tumor catalytic materials with abundant active sites, high catalytic efficiency and accurate tumor tissue recognition to utilize the limited therapeutic reaction materials and obtain the optimal therapeutic effect with the lowest toxicity, which has become an active new frontier of cancer treatment [19].

Notably, the tumor-destroying ability and toxicity of nanocatalytic materials are symbiotic, both derived from metal atomic sites in catalysts. In particular, the potential toxicity of dissolved ions to normal tissues is the main reason that hinders their practical clinical application. To break through this bottleneck, several strategies have been explored, such as targeted delivery of nanomedicines and controlled release of metal ions. However, most nanoparticles are randomly distributed in organs after intravenous injection and continuously release trapped metal ions, eventually leading to cell death. Until now, the method of increasing the metal atomic efficiency is perhaps the most fundamental solution to the toxicity of catalysts. Since Zhang and coworkers first immobilized isolated Pt onto FeO_x substrate surface in 2011, single-atom catalysts (SACs) are considered to be the limit of elaborate synthesis at the atomic level, have become the brightest stars in catalysis [20–27]. When the catalyst realizes an atomic distribution, its surface free energy, quantum size effect which is the unique HOMO-LUMO gap and the discrete energy level distribution, and metal-carrier interactions between the supporting substrate and the single atom all undergo promising changes [28–30]. Thanks to the unique electronic structure that facilitates charge transfer and the unsaturated coordination environment of isolated single atoms, SACs not only possess extremely uniform microstructure and active site distribution, but also exhibit excellent catalytic activity and ideal selectivity [31–36]. The appeal advantage allows SACs to maximize the

use of metal atoms and achieve satisfactory cancer treatment results at relatively low metal concentrations [37–42]. Importantly, the active sites are easy to accurately identify and characterize, which facilitates the further elucidating and understanding of the structure-performance relation and the catalytic mechanism, thus facilitating the oriented and rational design of more advanced SACs [43–47].

Although SAC has unique advantages, it still has limitations that restrict its broader development. (1) Since SACs has only one specific active center, in complex reactions involving multiple intermediates, the same adsorption site cannot make all intermediates reach the best adsorption state, that is, it is hard to conquer the linear relationship among intermediates, which reduces the selectivity of the target product and fundamentally limits the catalytic efficiency. (2) Because of the high surface energy of isolated metal atoms, the metallic loading of SACs is usually limited to 1 wt%–2 wt% to sustain the atomic structure. Forcing up the load will cause the agglomeration of metallic atoms to form nanocrystals, which will break the dispersive properties of the single atom on the surface. Therefore, even if the atomic utilization of SACs can achieve 100%, it is still difficult to obtain the best catalytic effect. (3) Since the single central metal atom of SACs is usually surrounded by non-metallic atoms such as C and N, it is difficult to further enhance its intrinsic catalytic activity. Recent studies have shown that dual-atom catalysts (DACs), as an upgraded version of SACs, fully retain all the advantages of SACs, but also develop more individual advantages, which can effectively break through these limitations of SACs [13,48–51]. When we only set the reactant molecules to be adsorbed on active sites without considering subsequent steps, the goal is to obtain the most stable adsorption structure by the lowest energy adsorption method. However, when the Sabatier principle considers both the catalytic activity and adsorption energies of key intermediates, the optimal adsorption mode should be moderate [52–54]. Too weak and too strong binding strength may not be conducive to reactant activation and product desorption, respectively. That is, lower adsorption energy is not better, which gives rise to the concept of volcano diagram. For instance, proton coupling and electron transfer following the adsorption process is commonly identified as the rate-determination step (RDS). Under this circumstance, the RDS energy barrier will increase with the



Jingqi Guan (Jilin University) was invited as a young member of the 6th Editorial Board of *Chin. J. Catal.* and the 5th Editorial Board of *Acta Phys.-chim. Sin.* Prof. Jingqi Guan received his B.A. degree in 2002 and Ph.D. degree in 2007 from Jilin University. He carried out postdoctoral research in the University of California at Berkeley from 2012 to 2013 and in Dalian Institute of Chemical Physics, Chinese Academy of Sciences from 2014 to 2018. His research interests are in engineering single-atom catalysts and 2D materials for electrocatalysis, renewable energy, and biosensors. He has published more than 180 peer-reviewed papers.

decrease of the adsorption structural energy, resulting in enhanced difficulty of reaction. Moreover, the adsorption strength of reactants and intermediates in SACs is difficult to control, while since the active sites of DACs are two adjacent metal atoms making them has a variety of active centers, including the top and bridge sites, and therefore they can provide more multiple adsorption methods for reactants (Fig. 1) [55–59]. In addition, DACs also have minimal bridging active sites, which allow neighboring atoms to cooperate more flexibly with each other, and thus the D-band centers can be regulated more efficiently *via* electron-orbit interactions, leading to higher optimized adsorption energies of intermediates on the active sites [60–63]. In this way, linear relationships that are unable to be avoided in SACs can be broken in DACs, leading to better overall catalytic performance, which implies more potential for future practical applications [64–67]. DACs are divided into two categories: homonuclear and heteronuclear based on the consistency of center metal elements. The former is the majority of the catalysts reported so far, such as Fe₂, Pt₂, Co₂, etc. loaded on graphene or alloy nanowires [68,69]. Inspired by bimetallic nano-catalysts, heteronuclear dual-atom catalysts (HDACs) formed by adding another isolated metallic atom have gradually become the center stage of recent research in this field due to their superior catalytic performance [70–76]. HDACs can be further divided into (1) mononuclear heterogeneous pairs [77–80] and (2) binuclear heterogeneous pairs [81–83]. In the former catalyst, the distribution of the two metal monatoms on the support is random, resulting in no definite range of distance between them, and therefore, they are rarely close to each other to form the M1-M2 configuration, thus unable to obtain the extremely important synergistic effect between the bimetallic atoms [84–86]. The following discussion focuses on the HDACs which possesses a remarkable synergistic interaction between the atoms with two different metal element that can greatly boost the catalytic activity and selectivity [71,87,88]. More importantly, these active sites of HDACs exhibit unique asymmetries and are thought to be dimers in a specific form in which the elements of the atoms are different [89]. Compared with monometallic DACs, these asymmetric active centers not only have significantly enhanced charge density gradients, but also locally generate torque beneficial to efficient overlap of atomic orbitals when activating reactive linear molecules [90]. In addition, compared with other types of SACs, which can only change the electronic state of one ac-

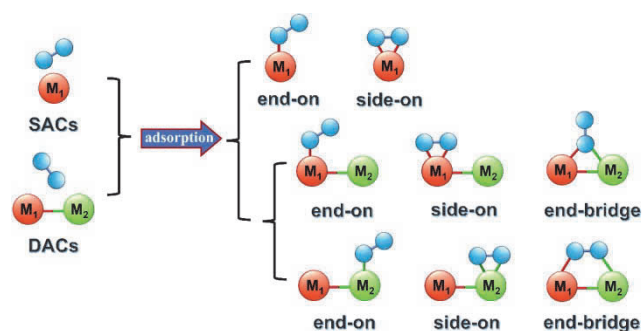


Fig. 1. Schematic diagram of adsorption configurations for single and diatomic sites (blue: adsorbed molecules, such as O₂ or N₂).

tive site, the asymmetry also endows HDACs a more flexible transition state of the active atom, and thus it is easier to break the linear limitation of the traditional SACs [91–94]. These exclusive advantages lead to satisfactory catalytic performance far superior to SACs and monometallic DACs for the activation of ROS-derived molecules such as O₂ and H₂O in the TME [95–97].

In this review, we first introduce various characterization methods for atomic-scale sites, discuss their main applications, and compare corresponding advantages and disadvantages. Secondly, we systematically reviewed the preparation strategies of bimetallic single-atom catalysts in detail, i.e., the traditional high-temperature pyrolysis method, wet chemical double solvent method, atomic layer deposition (ALD) technique, and soft template self-assembly technique, and the corresponding applications of the related catalysts are briefly described. Subsequently, we mainly introduced HDACs that are highly effective in anticancer through Fenton/Fenton-like reaction or other mechanisms [98]. Finally, we proposed possible challenges and prospects for future application. We hoped that this paper can offer some systematic insights into the development of bimetallic atomic catalysts and promote related technologies.

2. Advanced methods for the characterization of DACs

To determine the structures of bimetallic single-atom sites in the target HDACs and to better understand the structural and functional synergies between two isolated single atoms as well as the single atom and the carrier, researchers have used a variety of characterization techniques combined with theoretical computational studies to reliably confirm the existence, spatial distribution and electronic structure of these isolated centers (Fig. 2) [28,99–101]. In the section, we give a concise introduction of multiple progressive methods for active site detection at the atom level, in particular *in situ/operando* methods such as high-angle annular dark-field scanning transmission electron microscopy (HAADF-STEM) [102–104], synchrotron radiation X-ray absorption fine structure (XAFS) [105–107], fourier transform infrared spectroscopy (FTIR) and Mössbauer spectroscopy (Table 1) [108–110].

2.1. Microscopy

To see ultrastructures below 200 nm that are invisible under conventional optical microscopy, shorter wavelength irra-

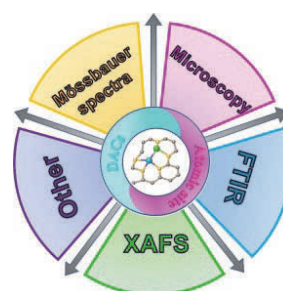


Fig. 2. Characterization techniques for SACs.

Table 1

Main characterizations for analyzing DACs.

Method	Purpose	Advantage	Disadvantage	Ref.
Microscopy (TEM, HAADF-STEM)	Direct imaging of metal elements with atomic resolution is used to detect the size and distribution of metal single atoms. The technique also provides relevant local structural information of atomic-level sites on the supporting material.	(1) Since the principle is based on Rutherford scattering, the image is bright enough to allow the observation of thick samples and low contrast samples. (2) Using the strong excitation and high-resolution imaging of the objective lens during the scanning transmission mode, microdiffraction can be achieved, which enables the visual observation of single atoms with 3D structure fixed in the N-doped graphene supporting framework.	(1) It can only provide regional imaging of a specified location, without the ability to observe a wide area. (2) Only the surface of the sample can be characterized, while the morphology and structure of the core material encapsulated in the shell materials with 3D structure cannot be observed.	[114, 128–131]
XAFS	Used to characterize the local geometric or electronic structure of a sample. It can elucidate the physical distance, coordination state, electronic structure and other highly accurate local information in atomic level.	(1) The overall structure can be determined by accurate <i>in situ</i> characterization of the single bimetallic atoms. (2) It can provide information about the stable adsorption structure and chemical bonding state of single atom on substrate materials. (3) The oxidation state and coordination number of the metal center in the complex can be characterized.	(1) Because X-rays are destructive, they can damage samples during measurements. (2) For XANES, there is the effect of multiple scattering emitted by photoelectrons and Auger electrons. Therefore, it is difficult to determine the identity of the oxidation states and scattering atoms.	[132–135]
FTIR	By monitoring the adsorption behavior of these highly responsive guest molecules, the dispersion status of atomic-level metal sites in functional carriers was evaluated.	(1) High sensitivity, samples even below 10 nanograms can obtain satisfactory FTIR spectrograms. (2) The sample preparation is simple, and the reflectance spectrum of the opaque sample can be measured directly. (3) In the process of analysis, the original morphology and crystal form of the sample can be maintained without any detriment of the sample.	The analysis of complex mixtures and aqueous solutions is complicated.	[136–140]
Mössbauer spectroscopy	Used to detect the coordination structure and electronic properties of materials such as oxidation states, spin states, chemical bond properties and other microscopic structure information.	(1) Mössbauer spectroscopy has extremely high energy resolution. (2) Because the Mössbauer effect involves resonant transition, the energy level structure, which depends on the chemical environment of the nuclear determines the shape and spectrum parameters, so it can reflect the change of the chemical environment around the resonant nuclear extremely sensitively. (3) Mössbauer spectroscopy has very little damage to the sample. (4) The test objects can be crystalline, amorphous, powdery or even frozen solutions, and the range of applications is extremely wide.	(1) Mössbauer spectroscopy is a volume technique that reflects the combined results of various sites in the material. (2) Only finite types of nuclei such as Fe and Sn have the Mössbauer effect, and must be carried out at low temperatures or in laboratories with preparation source conditions, which limits its application.	[141–145]

diation sources are applied to improve the resolution. In 1932, Ruska contrived transmission electron microscope (TEM) with electron beam as light source. The TEM resolution can reach the ultra-small magnitude of 0.1–0.2 nm, thus magnifying the observed sample by millions of times. Therefore, TEM enables the observation of structures as fine as just a row of atoms, making it the best choice for the precise observation of microscopic morphologies of nanomaterials [111,112]. On the basis of TEM, HAADF-STEM use a ring detector around a central electron beam to collect high-angle scattered electrons from the sample for imaging [113]. These factors make HAADF-STEM is sensitive to changes in the atomicity [114]. As for atomic-level sites in DACs, HAADF-STEM images with aberration correction to improve image clarity can easily identify diatomic sites and visually determine their spatial distribution according to different Z values of active sites and carrier elements. Furthermore, electron energy loss (EELS) spectra can be obtained by linear/planar scanning of the HAADF-STEM to further characterize the element dispersion.

2.2. XAFS characterization

Different from the material structure detection techniques so far, which are generally based on the diffraction phenomenon of the long-range ordered crystalline structure, XAFS is ground on the scattering phenomenon of the outgoing photoelectrons from the central absorbing atoms by the neighboring atoms [115,116]. This makes XAFS can be applied to both crystal and non-crystal, and become an ideal choice to explore local structures of catalysts. XAFS can be subdivided into extended X-ray absorption fine structure (EXAFS) and X-ray absorption near edge structure (XANES). The former is the oscillation of the X-ray absorption coefficient of an element in the range of 30–1000 eV at the high-energy side of the absorption edge, which can be used to explore the detailed structure. XANES is the fine structure within 50 eV of the elemental absorption edge, which can provide us with chemical valence. In the XAFS measurements, before probing a sample, we tune the X-ray

energy to match the internal electron shell of the target element, and then collect the absorbed X-ray amount and discuss its energy dependence [117,118]. It can help researchers to identify the dynamic structure/bond state evolution of reaction centers under working conditions. Combined with Fourier transform (FT) analysis, XAFS can effectively provide key information structure, including the coordination number, bond length, center of metal oxidation state, the atomic arrangement, even electronic structure, making the existence of this technique in identification of crystal defects and distortion as well as the crystal strain or additional dopant influence of diatomic active sites [119]. In addition, the FT is further complemented by the wavelet transform (WT), which can distinguish the backscattered atoms even if the adjacent bonds have a large overlap in R-space [120,121].

2.3. FTIR spectroscopy

FTIR is non-deviated and its core portion is a dual-beam interferometer that Michelson interferometer is commonly used. When the eyepiece is shifted, the difference of the optical path between the interfering beams will alter, and the detected light intensity will also change, thus obtaining the interference spectrum. When guest molecules are absorbed onto carriers with active sites at various atomic levels, they usually exhibit different vibration frequencies and intensities. FTIR can be used to monitor the adsorption process of highly responsive target molecules like CO to evaluate the metallic atom dispersion state in charge carriers. FTIR measurement has the following advantages: (1) the signal-to-noise ratio is improved by multi-channel measurement; (2) there is no limit to the incident and exit slit, thus high luminous flux, improving the sensitivity of the instrument; (3) on the basis of helium, neon laser wavelength, wave numerical precision can reach 0.01 cm; (4) the resolution can be improved by increasing the moving distance of the moving mirror; (5) the working band can be extended from the visible region to the millimeter region, so that the determination of far infrared spectrum can be realized [122].

2.4. Mössbauer spectroscopy

In 1956, Mössbauer [123] summarized the previous studies and pointed out that some radioactive nuclei in solids had a certain probability to emit gamma (γ) rays without recoil, and γ photons carried all the nuclear transition energy. The γ -rays emitted by the same nucleus in a solid in the ground state also have a certain chance of being absorbed by resonance without recoil. This emission or resonant absorption of γ -rays from nuclei without recoil became known as the Mössbauer effect, which is also the basic mechanism of the Mössbauer spectroscopy. According to the appeal introduction, when no recoil γ -rays radiate through an absorber, if the incident γ photon energy is consistent with the level transition energy of the target nucleus, the photon corresponding to this energy will be absorbed by the absorber resonance [124]. Mössbauer spectrum can be classified into singlet, doublet and sextuplet constituents to detect doublet states including low (D1), medium

(D2), and high (D3) spin states, which is universally accepted evidence of the presence of M-N_x sites. Furthermore, many valuable information can be obtained from Mössbauer spectrum, such as the types, electronic states and bonding conditions of the metals in DACs. For example, Wu *et al.* [125] obtained a better understanding of the coordination environment of the Fe-Co double site with the help of Mössbauer spectroscopy. In the Mössbauer spectra of Fe-Co DAC, in addition to the typical triplet signals, a small number of singlet components appear, which positively indicates the existence of Fe–Co bond (Figs. 3(a), (b)). Furthermore, for Fe,Mn/N-C, D4 instead of D3 and singlet components can be observed, D4 belongs to the unsaturated N-(Fe^{III}N₄) structure, which enabled Fe,Mn/N-C DAC to be catalytically reactive (Fig. 3(c)) [126]. However, this method still has obvious shortcomings. Up to now, merely 42 elements have been found to have Mössbauer effect. In particular, no chemical element containing Mössbauer that is lighter than potassium (K) has been found. Most of the discovered nuclear transitions can be observed at low temperature. So far, only 14.4 keV of Fe and 23.87 keV of Sn have a high probability of Mössbauer effect at room temperature and have been fully applied. However, for the solid without Mössbauer atoms, some suitable Mössbauer nuclei can be artificially introduced into the solid to be used as probes for indirect research, and many useful information can also be obtained [127].

2.5. Other methods

Besides the basic characterization methods described above, there are several related methods that have not been widely used, including the electron spin resonance (ESR) measurement and magic-angle spinning-nuclear magnetic resonance (MAS-NMR), etc. For the transition from low to high energy states of the nucleus, the energy (ΔE) is absorbed. Nuclear magnetic resonance (NMR) spectra based on this principle can provide valuable information about metal-bound ligands, such as coordination structure and chemical shifts, for the characterization of DACs [146,147]. Using this information, the location of the atomic metal center on the substrate can be inferred. For example, Yan *et al.* [148] used MAS-NMR spectroscopy to characterize the monoatomic platinum catalyst supported on mesoporous alumina (Pt-Al₂O₃). Three signals at 70, 38 and 7 ppm, can be clearly observed in the spectrogram, corresponding to tetrahedral (AlO₄), pentahedral (AlO₅) and octahedral (AlO₆) coordinated Al³⁺ species, respectively. In contrast, commercial Al₂O₃ has only two signals located at 10 ppm and 70 ppm, indicating the existence of pentahedral coordinated Al³⁺ species in the prepared samples. Furthermore, based on the recovery time and multi-quantum (MQ) NMR measurements of Al³⁺ species, it was shown that this structure accounted for more than one-third in the final sample (Figs. 3(d)–(f)). Thus, the unsaturated five-coordination structure of Pt-Al₂O₃ is successfully determined, and the single Pt atom is fixed on γ -Al₂O₃ by oxygen bridge.

Electron paramagnetic resonance (EPR) relies on the magnetic moments of unpaired electrons. Because the free radical orbital magnetic moment contributes nearly nothing, the total

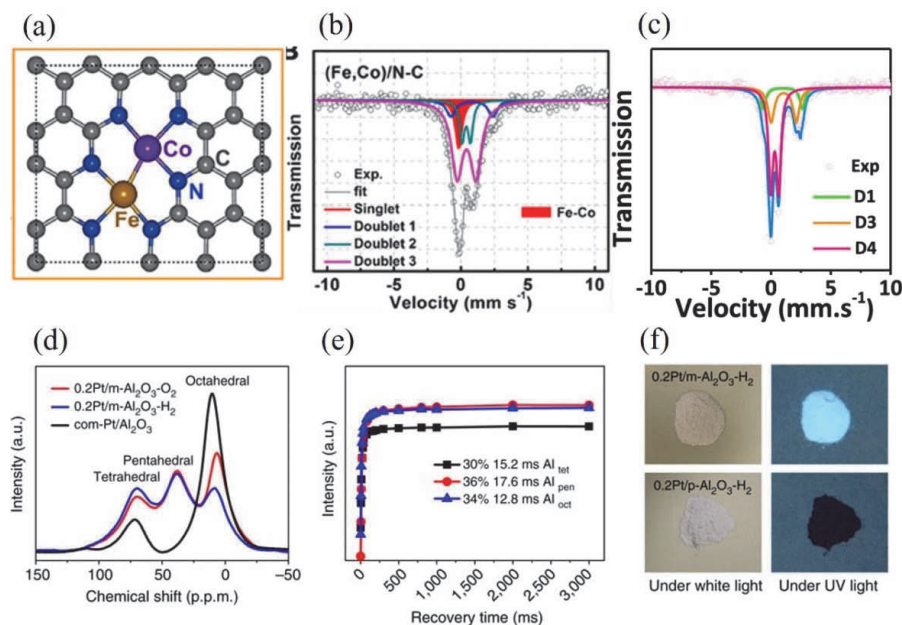


Fig. 3. (a) Fe-Co dual-site structure. Mössbauer spectra of Fe,Mn/N-C (b) and Fe,Mn/N-C (c) under room-temperature. (d) Al MAS-NMR spectra. (e) Intensity changes. (f) Photographs of Pt-Al₂O₃ samples under white light and UV light (365 nm). (a,b) Reproduced with permission [125]. Copyright 2017, American Chemical Society. (c) Reproduced with permission [126]. Copyright 2021, Springer Nature. (d–f) Reproduced with permission [148]. Copyright 2017, Springer Nature.

magnetic moment is mainly from the electron spin. Therefore, EPR also known as electron spin resonance (ESR), plays the role in understanding the evolution of the free radical on the surface of catalysts during the reaction process, providing valuable fingerprint information of captured electrons or carrier vacancies. For example, the unpaired $3d^9$, $S = 1/2$ electron configuration of Ni(I) of the monatomic Ni catalyst was determined by EPR technique at -196 and 25 °C with g values of 2.285 and 2.215, respectively [149]. As reported in the relevant literature, the partially occupied $3d_{x^2-y^2}$ orbital makes the isolated Ni(I) species highly reactive and is widely recognized as the catalytic active site. However, these Ni(I) species are not stable at high temperatures and typically produce Ni(II) and Ni(0) disproportionately. The low electronegativity (S and pyridine N) make the Ni(I) sites stable on the carrier. Given the ubiquitous type of electron paramagnetic coordination in DACs, it is expected that the ESR results will provide strong evidence to identify the atomic structure.

3. Preparation methods of HDACs

Bimetallic HDACs are different from monometallic homonuclear DACs in that their diatomic active sites are made of different metals that can theoretically be of rich combination types. The different diatomic active sites of HDACs have more regulatory interactions on the electron coordination environment and the adsorption energy of surface reactive species, thus providing the possibility of obtaining even more unexpected properties [150–153]. This is because there is a “see-saw” phenomenon between the single atom active sites of different metals. Understandably, the above-mentioned synergies, which are the main source of the improved catalytic perfor-

mance, are weakened as the distance between the two metal sites increases. The high surface free energy and inaccessible dynamic behavior of the reactive atom as well as the weak binding to the support make HDACs extremely unstable during the synthesis process. Once the distance between the double active metal atoms becomes close, agglomeration will inevitably occur, resulting in the formation of alloys or large size nanoparticles. In view of these challenges, the exploration of overcoming these obstacles to achieve accurate and controlled synthesis of HDACs has been the research focus in this field, and a lot of efforts have been made [154]. So far, four main methods for HDACs synthesis have been explored, including the traditional high-temperature pyrolysis method and the interesting wet chemical double solvent method [155], sequential atomic layer deposition (ALD) technique [156–158], and soft template self-assembly technique (Fig. 4) [159–162].

3.1. High-temperature pyrolysis method

High-temperature operation with mature technology is the most commonly used method to synthesize all kinds of DACs [166–169]. Simply speaking, the metal precursor of the target product is mixed with the carbonaceous material as the supporting substrate and then pyrolyzed [170,171]. However, due to the instability under high temperature, a series of different catalytic site configurations outside the ideal dual-atom structure will be generated, such as the single metal sites, irregular metal sites of mononuclear DACs and even small part of agglomeration. Therefore, the temperature of pyrolysis should not be set too high, generally in the range of 700 to 1000 °C [167,172,173]. Furthermore, the selection of pyrolysis atmosphere, including N₂, Ar, H₂ and NH₃, also has a remarkable im-

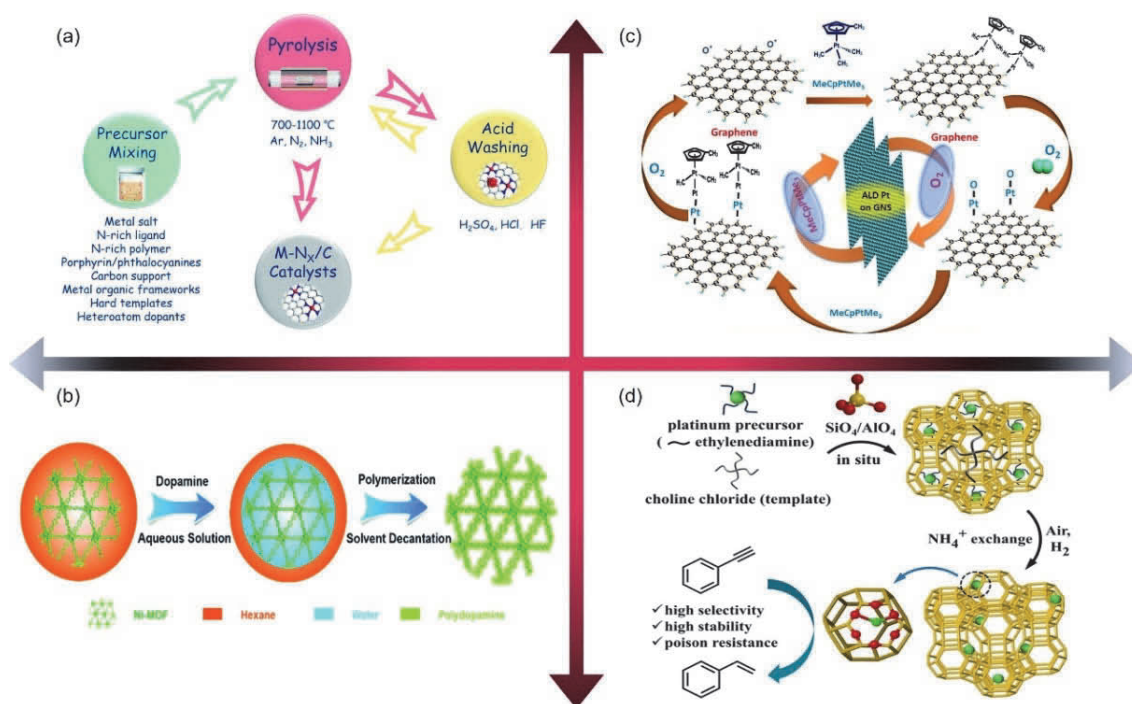


Fig. 4. Schematic diagrams of the mechanisms of typical high-temperature pyrolysis (a), wet chemical double-solvent (b), Pt ALD mechanism on graphene nanosheets (c) and soft template self-assembly methods (d). (a) Reproduced with permission [163]. Copyright 2021, Royal Society of Chemistry. (b) Reproduced with permission [155]. Copyright 2018, Royal Society of Chemistry. (c) Reproduced with permission [164]. Copyright 2022, Elsevier. (d) Reproduced with permission [165]. Copyright 2022, John Wiley and Sons Ltd.

impact on the micro-morphology, activity, stability and so on. In addition, it is often followed by a subsequent acid etching process to remove the accumulated nanoparticles. Here, pyrolysis can be further divided into two types according to whether to contain the inclusion of specified precursors such as special metal-organic framework (MOF) [174] and its derivative zeolitic imidazolate frame (ZIF) based complexes [175], irregular biological premise complexes [176], etc.

3.1.1. Containing MOF/ZIF pyrolysis method

MOFs are a type of polymer materials that have flourished in recent years. They are commonly connected by metal ions and organic ligands to form porous three-dimensional extended structures (Fig. 5(a)) [28,177–181]. It is worth mentioning that nanomaterials with Fe-N-C coordination structure have been a hot research frontier since the first discovery of their excellent catalytic activity in 1964 [182]. In this regard, the well-defined morphology of MOF rich in pores can not only provide ultra-high surface area but also easily adapt various guest objects including metal salts, quantum dots, etc. In addition, by introducing organic linkers of different types and functions between metal nodes for post-modification, the structure of MOF can be flexibly customized to match the target reaction species [94,174,183,184]. Moreover, compared with other synthesis methods, the synthesis based on MOF enables to accurately dope metal atoms while retaining high porosity, which can promote the mass transfer of the reactants, making great contribution to the electronic structure optimization, thus causing obviously reduced energy barrier during the catalytic process. In particular, when preparing DACs with the coordina-

tion of N, because of the competition between agglomeration of metal atoms and metal-nitrogen bonding, the latter will be preferred during the pyrolysis process, which subtly reduces the probability of agglomeration. These advantages enable MOF to effectively host bimetallic active atoms and provide them with a strong coordination environment to ensure that the final HDACs exhibits more efficient and durable catalytic performance [185]. For example, Cao *et al.* [186] successfully embedded Fe and Mn atoms in N-doped porous carbon materials with Fe-N₄-Mn-N₃ heteroatomic coordination structure. HAADF-STEM images revealed clear and intuitive distribution of Fe/Mn dual sites. From Fig. 5(b), a series of bright spots correspond to the single Fe/Mn atom, most of which are uniformly dispersed in the form of double sites. Combined with the intensity distribution statistics, it can be further analyzed that the distance between heterogeneous single-atom sites is about 2.4 Å (Fig. 5(c)). From Mössbauer spectroscopy, the shortage of Fe crystalline phase of Fe⁰ carbide phase and the Mn atom doping greatly affect the properties of Fe-N_x (Fig. 5(d)). As for Fe-Mn-N-C, XANE and EXAFS were applied to further detect the valence states and structure of diatomic sites. As shown in Fig. 3(d), the signal peak between FePc and FeO is nearer to FePc, suggesting that Fe element is in +2 valence state, which ideally corresponds to the highest proportion of singlet state in Fe Mössbauer. However, the edge positions of them are apparently shifted, which is mainly caused by various symmetries, coordination atoms and other factors surrounding Fe. The main peak of the Fourier transform (FT) EXAFS peak of Fe is located at 1.44 Å, and the secondary peak appears at 2.25 Å, representing the isolated Fe–N (O) bond and the next closest metallic

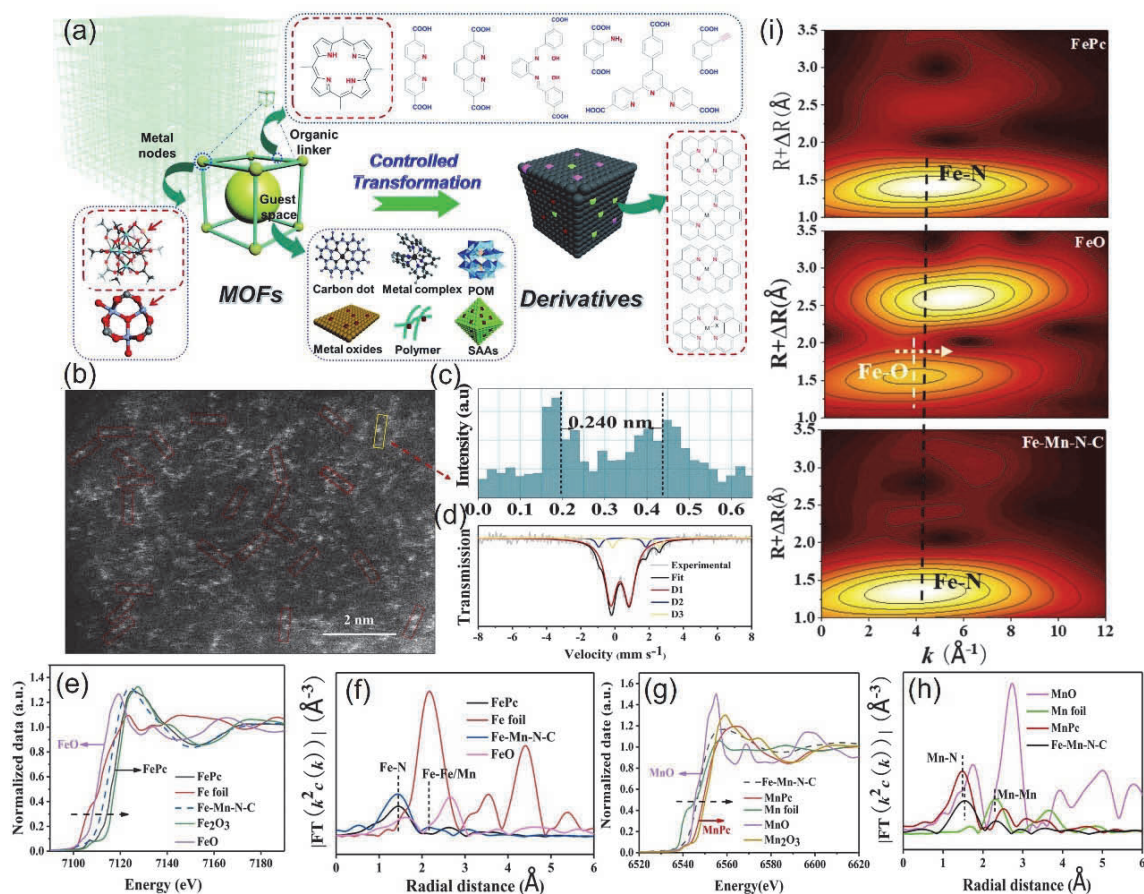


Fig. 5. (a) Schematic diagram of various construction strategies of MOF-based SACs. HAADF-STEM image of Fe-Mn dual sites (b) and corresponding intensity profiles (c). (d) Fe Mössbauer spectrum. Fe (e) and Mn (g) K-edge XANES spectra. Fe (f) and Mn (h) Fourier-transform EXAFS spectra. (i) WT of the k^2 -weighted EXAFS data. (a) Reproduced with permission [28]. Copyright 2020, Royal Society of Chemistry. (b–i) Reproduced with permission [186]. Copyright 2022, Elsevier.

bond, respectively. In addition, both the position and shape of the Fe curve in Fe-Mn-N-C are similar to those of FePc, meaning that the Fe atoms mainly exist in Fe-N(O) coordination structures. Furthermore, the Mn XANES position also has a near-edge absorption similar to that of Mn-O, indicating Mn²⁺. The Mn FT EXAFS reveals that the Fe-Mn-N-C main peak and secondary peak can be attributed to the Mn-N and Fe-Mn, respectively (Figs. 5(e–h)). The wavelet transform (WT) spectra further confirms that Fe/Mn species exists as Fe-N/Mn-N rather than Fe-O/Mn-O. Moreover, the bond length of fitted Fe-Mn ($2.42 \pm 0.02 \text{ \AA}$) is consistent with HAADF-STEM images (Fig. 5(i)). Combining the results of the above advanced characterization methods, it can be thoroughly identified that Fe and Mn atoms are mainly embedded in N-doped carbon (NC) in the form of FeN₄-MnN₃. Unlike other synthesis methods such as atomic-layer loading, mass-selective soft loading and defect engineering strategies, coordination interaction as well as space-limited design are the characteristics of MOF-based synthesis strategies for SACs [28].

Wang *et al.* [187] chose Zn/Co bimetallic MOF material as the substrate, and the Fe³⁺ precursor used as the guest metal source was firstly encapsulated in the cavity of Zn/Co MOF material by dual solvent method. Subsequently, under inert nitrogen atmosphere, the bonding between Fe³⁺ and Co node

atoms in the MOF was precisely regulated by a simple annealing operation at 900 °C, and Fe-Co bimetallic single atom sites were successfully embedded in the carrier. With the continuous growth of Fe-Co double sites, the initial rhombic dodecahedron substrate will gradually transform into nitrogen-doped CNT. The (Fe,Co)/CNT with excellent ORR catalytic performance was finally obtained (Figs. 6(a) and (b)). The magnified HAADF-STEM image (Fig. 6(c)) exhibits the dominant dual-metallic sites and the EELS demonstrates that Fe and Co sites coordinate to N at atomic scale (Fig. 6(d)). Through theoretical calculations, it was found that the O–O bond is greatly weakened at Fe-Co dual-metal sites, resulting in the surprising catalytic performance in activating oxygen (Figs. 6(e)–(g)) [187]. Yao *et al.* [188] reported a Co-Pt monoatomic co-embedded NC catalysts denoted as A-CoPt-NC. It was prepared from rod-like Co-MOF *via* a simple two-step synthesis strategy (Fig. 6(h)). Firstly, dicyandiamide was selected as the nitrogen source and mixed evenly with Co-MOF, and then placed in nitrogen atmosphere for high temperature annealing of 850 °C to achieve both the purpose of carbonization and nitrogen doping, and the Co-NC was obtained. Secondly, [189] an applied circulating voltage was applied to the Co-NC electrode using Pt electrode as the counter. In this process, the amorphous carbons are shoveled out and channels in the graphite carbon shell are

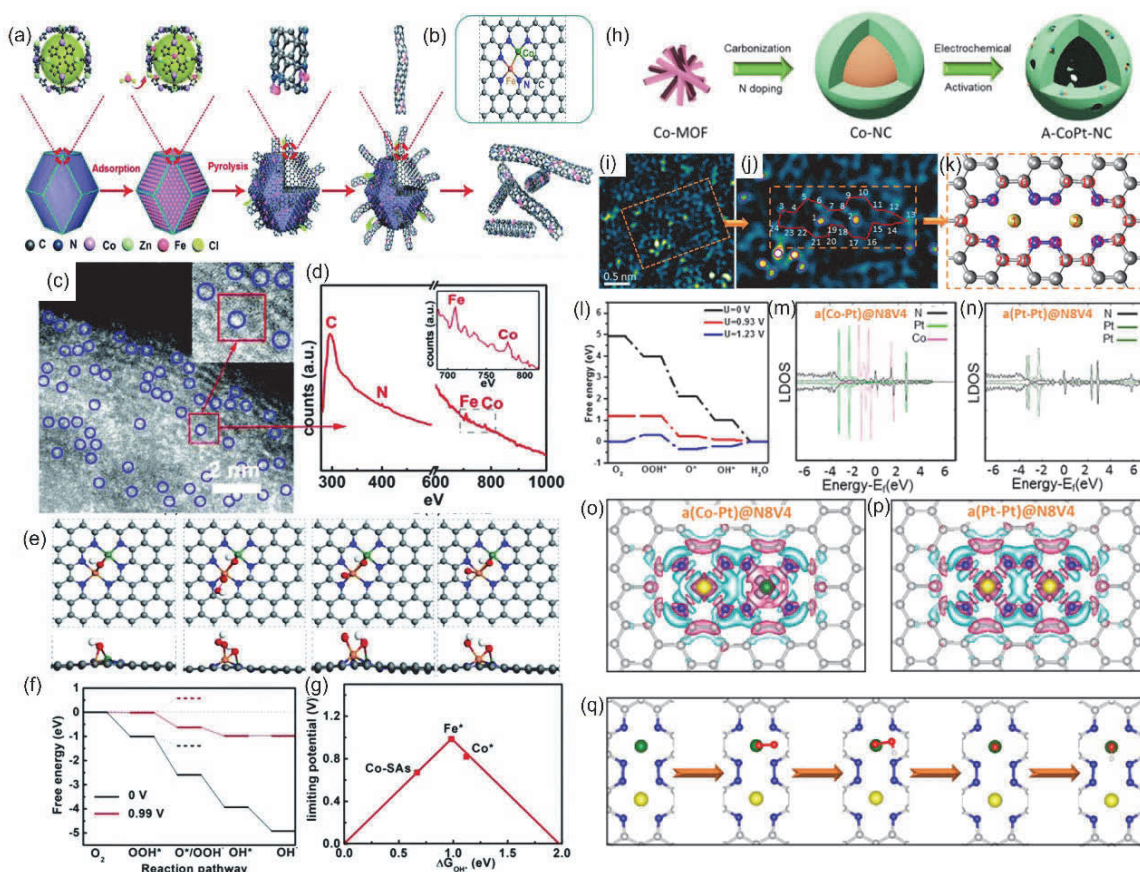


Fig. 6. Schematic diagrams of the synthesis of (Fe,Co)/CNT (a) and the structure of Fe-Co sites (b). HAADF-STEM image (c) and the EELS (d) of (Fe,Co)/CNT. Various intermediate geometric structures (e) and ORR free energy diagram (dashed line: the traditional $2e^-$ pathway) (f) on (Fe,Co)/CNT. (g) Relationship between ORR activity and ΔG_{OH^\bullet} . Co-SAs: Co site of bare Co SAs/N-C. Synthetic illustration (h) and HAADF images (i, j) of A-CoPt-NC. (k) Bimetallic atomic configuration model derived from the (h) region. (l–q) Theoretical calculation results of A-CoPt-NC. (l) ORR free energy diagram of (Co-Pt)@N8V4. Local state densities (m, n) and charge density vertical views (o, p) of (Co-Pt)@N8V4 (m, o) and (Pt-Pt)@N8V4 (n, p). (q) ORR pathway on (Co-Pt)@N8V4. (a–g) Reproduced with permission [187]. Copyright 2018, Royal Society of Chemistry. (h–q) Reproduced with permission [188]. Copyright 2018, American Chemical Society.

formed that allow acidic solvents to enter, thereby gradually removing the Co core from the initial Co/C core-shell structure. In addition, atomic Co sites are recaptured in the NC shell and some Pt atoms dissolved in the electrolyte from the Pt counter electrode can also be simultaneously captured. Therefore, N-doped carbon-based materials co-modified by Co/Pt at atomic scale were successfully synthesized. The HAADF image clearly shows that the two atomic metals are trapped in the vacancy defect, forming the atomic Co-Pt-NC coordination structure (Figs. 6(i)–(k)). As for ORR, unlike the $2e^-$ pathway of most Pt-based catalysts reported so far, A-CoPt-NC showed $4e^-$ ORR with specific and mass activities 85 and 267 times that of Pt/C, respectively. Combined with the results of DFT calculations, it is found that this high activity is not only from the synergistic effect caused by the asymmetry of electron distribution around the Pt/Co metallic centers that results in the upward shift of d band and charge redistribution to further accelerate the dissociation of water, but also due to the local coordination effect between metal atoms and NC substrate caused by the N8V4 vacancy in the carbon shell (N8: N atom number, V4: vacant C atom number), which together enhance the catalytic ability of this HDAC (Figs. 6(l)–(q)).

ZIF is a special type of MOF, in which organic imidazolate is cross-linked to the corresponding metal atoms to form a tetrahedral framework porous crystal material [190–192]. Because of its richer pores and stronger regulation of composition and structure, it can be used as a sacrificial template, molecular cage or metal-containing porous N-doped carbon material thus becoming an ideal precursor for the high-temperature pyrolysis synthesis of highly active DACs. It is worth mentioning that ZIF-8 [175,191,193] and ZIF-67 [194–197] synthesized from 2-methylimidazole and hydrated zinc nitrate precursors have been proven to efficiently derive in-plane adjacent HDACs by encapsulating metal precursors. Zhang *et al.* [198] successfully embedded a large number of homogeneous Co/Ni bimetallic monoatomic sites in the porous Janus-like NC framework by pyrolysis carbonization of ZIF-67 and nickel complex precursors with two different topologies (Figs. 7(a) and (b)). Specifically, the nickel precursors are tris-1,10-phenanthroline nickel(II) nitrate and dimethylglyoxime nickel(II), denoted as PNi and DN_i, respectively. Structural characterization revealed the unique microstructure of the final CoXNi-N/C and confirmed the uniform distribution of heterogeneous bimetallic single-atom active centers. The abundant micropores and nitrogen

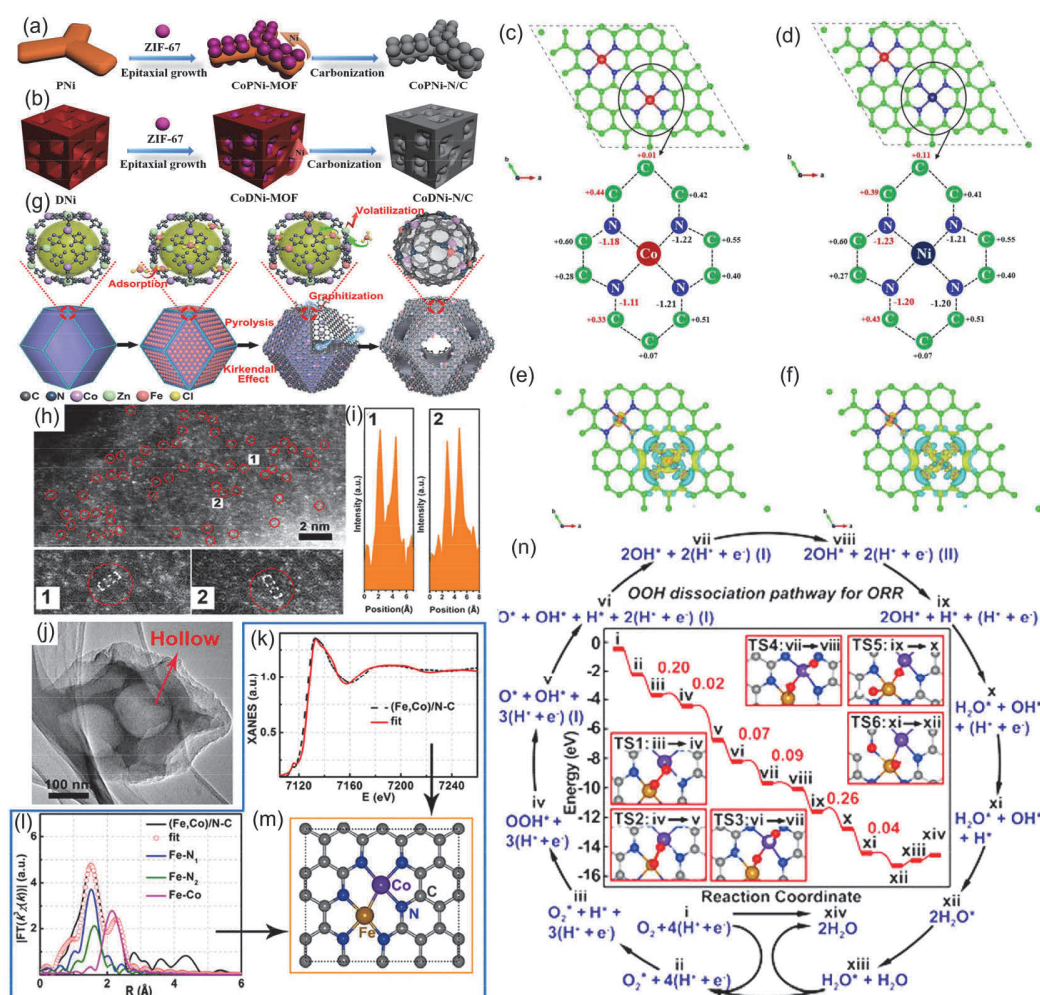


Fig. 7. Synthetic illustration of CoPNI-N/C (a) and CoDNI-N/C (b). Change of Bader charge in Co-N/C (c) and Co/Ni-N/C (d). Average electron density difference in plane between Co-N/C (e) and CoXNi-N/C (f) (yellow regions: the electron accumulation, cyan regions: the electron depletion). (g) Synthetic illustration of (Fe,Co)/NC. (h) HAADF-STEM images of (Fe,Co)/N-C (red circles: Fe/Co bimetallic active site). (i) Intensity profiles of corresponding zoomed areas in (h). (j) HRTEM image; XANES spectra (k) of (Fe,Co)/N-C and corresponding Fe EXAFS fitting data (l). (m) The structure of Fe-Co dual sites. (n) ORR intermediate and transition state energies of (Fe,Co)/N-C. (a–f) Reproduced with permission [198]. Copyright 2019, Elsevier (g–n) Reproduced with permission [125] Copyright 2017, American Chemical Society.

content, as well as the multi-effect synergistic effect between the newly introduced Ni and Co atoms, make the material exhibit outstanding catalytic performance under acidic/alkaline media. In addition, density functional theory (DFT) calculations showed that two types of N possess 1.18 and 1.11 electrons in the Co-N/C, respectively, while in the CoXNi-N/C or CoDNI-N/C systems, they are increased to the corresponding 1.23 and 1.20 electrons. This indicates that the Ni-N bond has obvious covalent characteristics, which can effectively enhance the electronic activity of N (Figs. 7(c)–(f)). Li *et al.* [125] designed a novel host-guest strategy to synthesize hollow carbon-derived HDAC with porphyrin Fe-Co bimetallic active sites ((Fe, Co)/NC) by combining the basic dual-solvent method and high temperature pyrolysis method (Fig. 7(g)). Specifically, they chose FeCl₃ as the Fe source to synthesize a Zn/Co MOF material, which is similar to ZIF-8 in the coordination structure of albite with a 2-methylimidazole organic skeleton linking Co²⁺ and Zn²⁺ bimetallic nodes as the host cavity molecule encapsu-

lating FeCl₃. This strategy is based on optimizing the bond state between the subject Co node and the subsequent adsorbed Fe node in the limited space of the ZIF-8-like urn molecule. First, the dual-solvent method effectively avoids the diffusion resistance caused by the narrow pore size (< 5 Å) of ZIF-8 structure, thereby completely encapsulating FeCl₃ in the abundant pores. Subsequently, the pre-product was pyrolyzed under Ar gas and 900 °C. During this process, the generated C atom reduced part of Fe³⁺ to produce an ideal check with the adjacent Co site. In turn, the adsorbed Fe³⁺ also catalyzes the release of N/C species from N-doped graphite carbon materials, thereby serving as a regulator of the geometry of the shell MOF material, making it easier to transport the associated catalytic reactants such as water molecules. In addition, according to Kirkendall effect, continuous carbonization and decomposition will further enlarge the size of ZIF-8 structure and the internal cavity, which is conducive to the embedding of more Fe nodes. The above processes can be confirmed by HRTEM,

HAADF-STEM and other morphological characterization methods (Figs. 7(h)–(m)). DFT calculation results reveal that the dissociated O atom has two types of Fe/Co anchoring sites, which leads to the reaction heat with greatly improved stability, and the strong bonding energy of O₂ at the bimetallic active site, thus fully activating O–O bond in the gas phase. This indicates that the O–O cleavage barrier at the Fe/Co double site is greatly weakened, making the O₂ molecule amenable to activation and thus achieving higher selectivity for the four-electron reduction pathway that exhibits superior catalytic activity (Fig. 7(n)).

3.1.2. Alternative pyrolysis method

The following discussion is about examples of using other porous packaging materials with special configurations other than MOF or ZIF as the substrate material to embed the corresponding metal single atoms on it through high temperature pyrolysis treatment. Due to different porosity and morphology of these substrate materials, the controllability of the synthesis process is not unified. The final HDACs using various techniques may exhibit a higher proportion of mutually remote non-synergistic single atom sites rather than the targeted state that two metallic single atom sites are adjacent to each other.

Sun *et al.* [199] designed a competitive complexation method to synthesize Zn and Co HDAC (Zn/CoN-C) based on pyrolysis. They selected chitosan as N-doped carbon substrate material, ZnCl₂ and Co(C₂H₃O₂)₂ as metal source. Since the electrons of 4s and 4p layers of the two metals can competitively complex with the –NH₂ and –OH groups on the chitosan molecules, the Zn and Co single atoms can be doped on the substrate surface with high uniformity. Subsequently, owing to the indiscriminate coordination ability of the two metal atoms, the atomic-level bimetallic sites were successfully obtained after pyrolysis at 750 °C, which can be confirmed by the XAFS characterization (Figs. 8(a)–(d)). In addition, DFT calculations showed a significantly extended O–O length from 1.23 to 1.42 Å, indicating that Zn/CoN-C has a strong adsorption capacity for the reactive species O₂, and the O–O bond cleavage is easier, making the ORR overpotential as low as 0.335 V (Figs. 8(e)–(i)). Zhao *et al.* [200] also used similar simultaneous competitive coordination pyrolysis method to prepare S-modified Zn and Co HDACs on a carbon-based material with a three-dimensional (3D) dentate morphology, noted as Zn,Co-N_x-CS_y (Fig. 8(j)). Since the doped S atom has a larger radius and smaller electronegativity than the N atom, defect sites will be generated by forming a porphyrin-like N₄ coordination structure which can be verified by

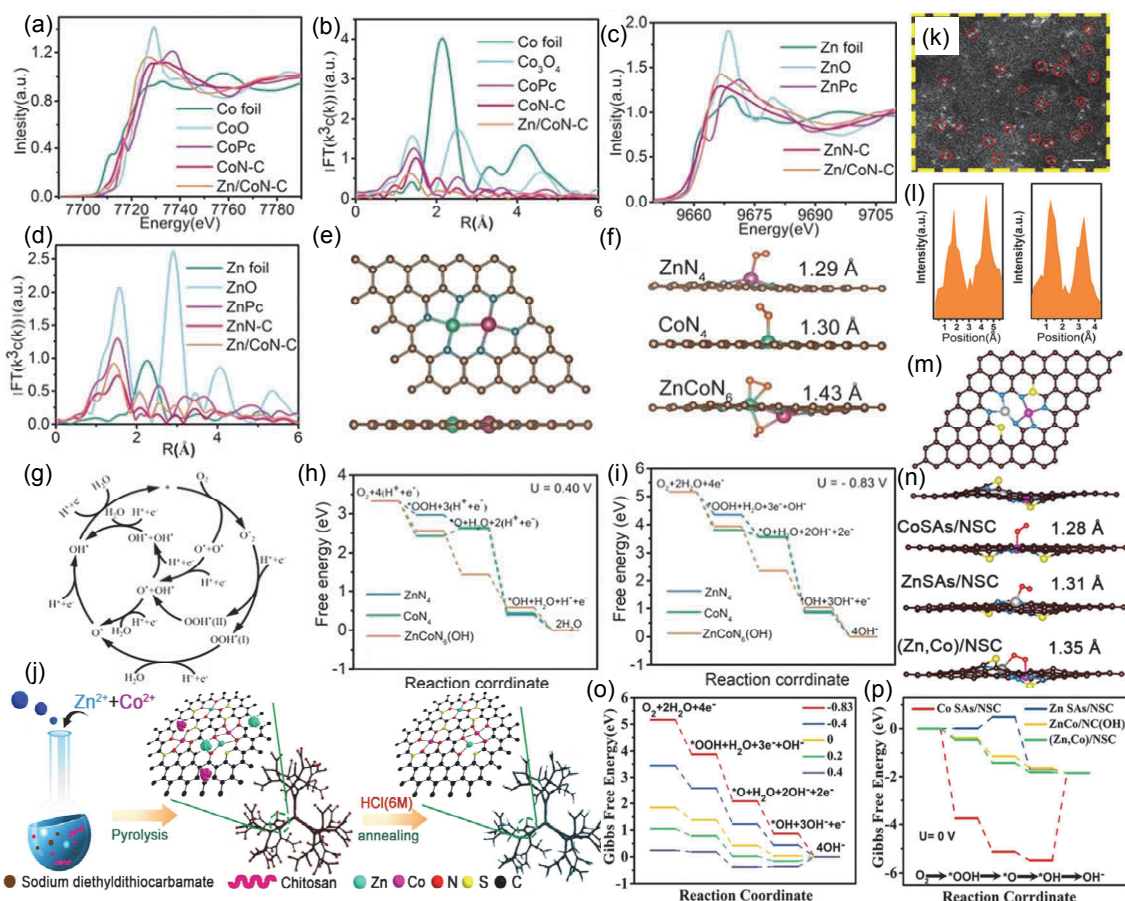


Fig. 8. XANES spectra of Co K-edge (a) and Zn K-edge (c). (b,d) FT EXAFS spectra of corresponding samples. (e) Optimized calculated geometry of the Zn/CoN-C. (f) Optimized adsorption configuration geometry of O₂. (g) Possible ORR reaction pathways in acidic environments. (h,i) ORR free energy diagram. Synthetic illustration (j) and HAADF image (k) of (Zn, Co)/NSC. (l) Corresponding intensity profiles. (m) Optimized calculated geometry of the (Zn, Co)/NSC. (n) Optimized adsorption configuration geometry of O₂. (o,p) ORR free energy diagrams. (a–i) Reproduced with permission [199] Copyright 2019, John Wiley and Sons Ltd. (j–p) Reproduced with permission [200]. Copyright 2019, Elsevier BV.

HAADF-STEM images (Figs. 8(k) and (l)), and the charge states around the active centers of Zn and Co can be redesigned to enhance their interaction with oxygen-containing substances, thereby beneficially regulating the active centers. Due to the large electronegativity difference between Co and Zn, the interaction between them will lead to a more optimized electronic structure and adsorption state of the pre-reaction/intermediate species. In addition, the results of theoretical calculation revealed that (1) the bond length of O₂ is extended from 1.23 to 1.35 Å to facilitate O–O activation. This makes the O₂ dissociation barrier much lower, thereby promoting the activation of the O–O bond in the step *OOH + e⁻ → *O + OH⁻. (2) The effect of doped S atoms to optimize the adsorption energy between Zn/Co single atom sites and reaction species can be attributed to their ability to reduce the energy barrier from *O₂ to *OOH (Figs. 8(m)–(p)).

Although the high temperature pyrolysis technologies introduced so far can be used to prepare the target bimetallic monatomic active sites, they need corresponding post-treatment operations to eliminate the undesirable pyrolysis species formed at the same time in the synthesis process, such as nanoparticles and oxides caused by agglomeration

phenomenon. Guo *et al.* [201] reported a novel ice-assisted photocatalytic reduction method without post-treatment operations to introduce Ru and Pt bimetallic single atoms to N-vacancy-rich g-C₃N₄ substrate surfaces with high coverage (Fig. 9(a)). HAADF-STEM and XAS characterizations confirmed abundant and adjacent Pt/Ru active sites. Firstly, N-vacancy-rich g-C₃N₄ was prepared by traditional high-temperature pyrolysis of g-C₃N₄ carbon material under N₂ atmosphere. Then, it was mixed evenly with the precursor metal salt of the precious metal Ru/Pt, and then rapidly frozen into ice with the liquid, and then irradiated with 300 W Xe light for 10 minutes until the ice melted naturally. The resulting solution was separated by centrifugation to obtain the final PtRuSA-CN620 product. In the process of introducing N into the carbon material by high temperature treatment, the maximum vertical dimension of CN is significantly increased from the original 4.20 to 5.47 Å, which leads to the high probability of synthesizing two adjacent Pt and Ru atomic sites (2.2 Å). Furthermore, the N-vacancy in the subtract material is a photo-generated electron-rich region, promoting the formation of isolated metal atoms. Compared with the structures of neighboring Ru-Ru/Pt-Pt monomers or isolated Ru/Pt atoms, noted

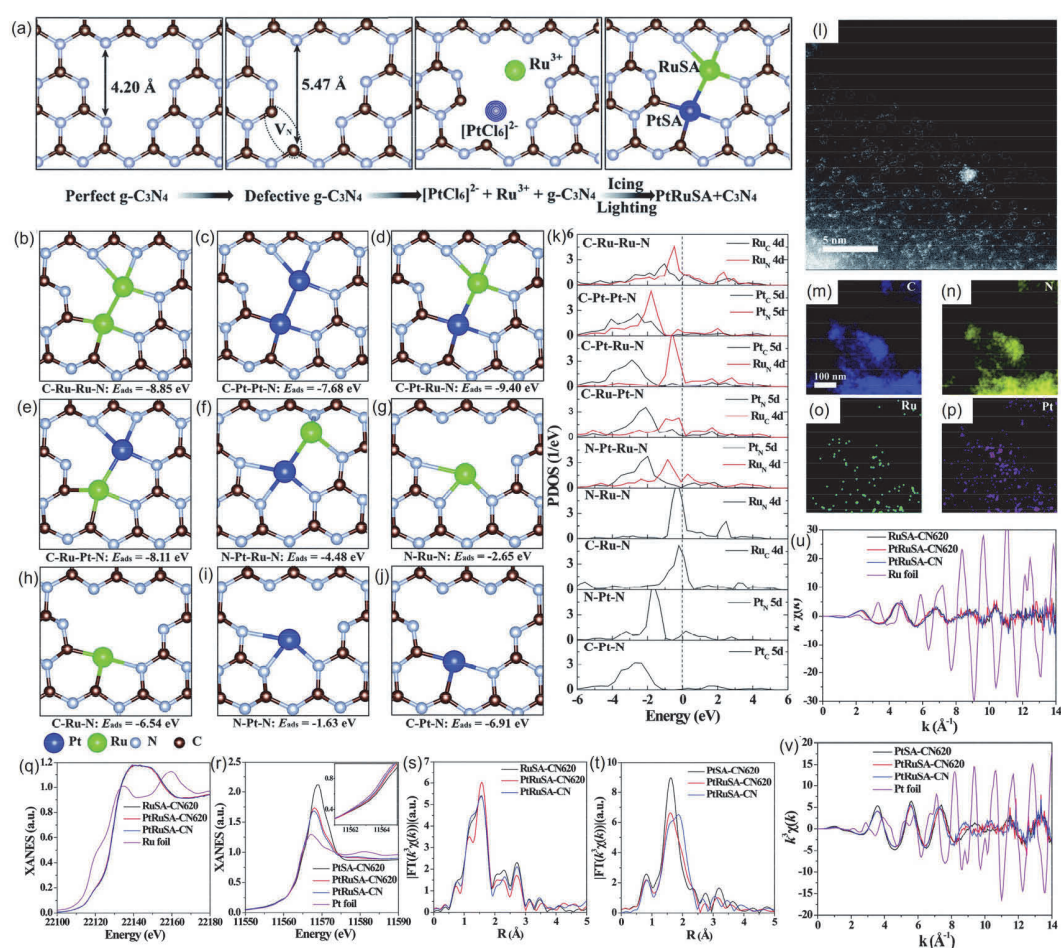


Fig. 9. (a) Schematic diagram of the ice-assisted photocatalytic reduction method. (b–j) The geometry structures of different samples. (k) PDOS plots. HAADF-STEM (l) and element maps (m–p) of PtRuSA-CN620. Ru K-edge (q) and Pt L₃-edge XANES (r) and FT spectrum of Ru/Pt at (s,t) R and (u,v) k spaces. Reproduced with permission [201]. Copyright 2019, Royal Society of Chemistry.

as C-M1-M2-N (M1/M2: Ru, Pt), the C-Pt-Ru-N model of the adjacent Pt-Ru monomer is thermodynamically stable, which paves a new pathway for the synthesis of novel atomically dispersed bimetallic catalysts (Figs. 9(b)–(v)).

3.2. Wet chemical double solvent method

The wet chemical method can be carried out under simple experimental conditions without the need for special experimental equipment and harsh operating conditions, which has become one of the easiest synthesis strategies [202–204]. When it is applied to the synthesis of HDACs, to effectively avoid the unfavorable agglomeration of single metal atoms to form nanoparticles or nanoclusters due to high surface energy, low concentration metal precursors have to be usually used. In 2012, Xu *et al.* [205] confined Pt species to the MIL-101 pores *via* a two-solvent path, greatly reducing the metal agglomeration on the MOF surface. Specifically, the dual solvents of the method include water and hexane [202,206]. The target metallic precursors with particles smaller than the pore size of porous urn materials such as MOFs were dissolved in water, while the substrate materials suspended in hexane, playing an im-

portant role in promoting the subsequent impregnation process.

For example, by exactly optimizing the bonding strength between Fe and Co in Zn/Co MOFs, Wu *et al.* [207] obtained (Fe,Co)/N-C catalysts with extremely uniform distribution of atomic active sites (Fig. 10(a)). In detail, the BMOFs material with Co^{2+} and Zn^{2+} metal nodes connected by 2-methylimidazole was selected as the substrate material. The Fe precursor metal salt was encapsulated in the pores of BMOFs by a double solvent method that Zn-Co BMOF was evenly dispersed in hexane by ultrasound firstly, then the $\text{FeCl}_3 \cdot 6\text{H}_2\text{O}$ aqueous solution was dropped to the above solution, and the thoroughly mixed slurry was stirred continuously at room temperature until the reaction was complete. Followed by annealing, Fe^{3+} and the original Co sites of the substrate formed a bimetallic single atom pair with the desired synergistic effect. The HAADF-STEM image clearly shows that the Fe-Co site is marked with blue circles, due to the different z values of the Fe-Co site compared to C and N, and does not show the characteristics of metals, metal oxides and metal carbides, indicating that the Fe-Co site is dominant. In addition, the EELS of a single Fe-Co site further confirms the coexistence of Fe and Co

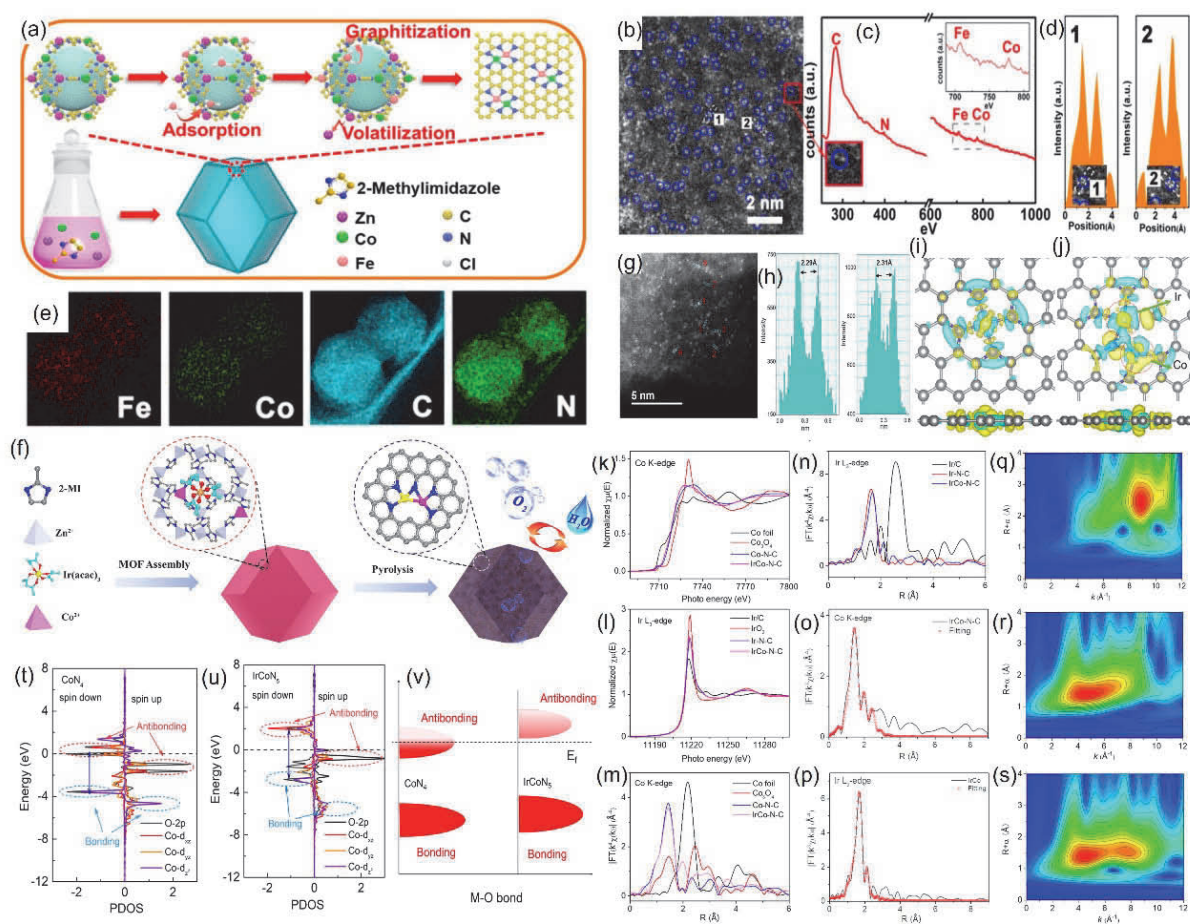


Fig. 10. (a) Synthetic illustration. (b) HAADF-STEM image. EELS spectrum (c) and corresponding contrast profiles (d) and EELS mapping (e) of (Fe,Co)/N-C. (f) Schematic diagram of the synthesis. HAADF-STEM image (g) and contrast profiles (h) of IrCo-N-C. Charge density diagrams of CoN_4 (i) and IrCoN_5 (j). XANES spectra (k,l), FT-EXAFS spectra (m,n) and EXAFS fitting curves (o,p) at Co K-edge (k,m,o) and Ir L_3 -edge (l,n,p). Ir L_3 -edge WT images for Ir/C (q), Ir-N-C (r), and IrCo-N-C (s). PDOS diagrams of CoN_4 -O (t) and IrCoN_5 -O (u). (v) Schematic bond formation of the Co-O bond. (a–e) Reproduced with permission [207]. Copyright 2020, American Chemical Society. (f–v) Reproduced with permission [208]. Copyright 2021, American Chemical Society.

at the atomic level. The high uniformity of the distribution of bimetallic monoatomic pairs on the MOF substrate material can be visually observed by the contrast profile of the Fe-Co site area. Thus, the Fe-Co sites are uniform and dominant in the HDAC (Figs. 10(b)–(e)). Similarly, Chen *et al.* [208] used this strategy to successfully obtain another HDAC: IrCo-N-C with asymmetric IrCoN₅ atomic pair structure (Fig. 10(f)). Firstly, a dual solvent method was used to synthesize precursors from Co-Zn BMOF substrates and Ir metal salts. The presence of Zn in BMOF dilutes the atomic site concentrations of Co and Ir, thus effectively inhibiting their aggregation and facilitating even dispersion of metal species. In particular, the two solvents they chose were both methanol, indicating that the choice of solvents in this strategy is not absolute, and there is room for further optimization in this direction. Subsequently, high temperature pyrolysis was carried out in an inert gas atmosphere

higher than 905 °C (the boiling point of Zn). In this process, a large number of new mesoporous structures were generated in the carbon matrix due to the pore foaming effect caused by the evaporation of Zn and the decomposition of ligand, which contributed to the full accessibility of related reaction species at the three-phase interface. The appellate views can be confirmed by physical representations such as HAADF-STEM, WT-XANES and FT-XANES images (Figs. 10(g)–(s)). In addition, the theoretical calculation revealed that the synergism between the bimetallic atom pairs, that is, the incorporation of Ir atom leads to the stronger spin polarization of Co site, enhances the binding affinity of Co site to O atom, and accelerates the oxygen activation (Figs. 10(t)–(v)). Lu *et al.* [209] successfully introduced non-noble metal-based Fe-Ni diatomic pairs on an N-doped graphene substrate with hollow spherical structure labeled Fe-NiNC-50 *via* one-step double solvent method with-

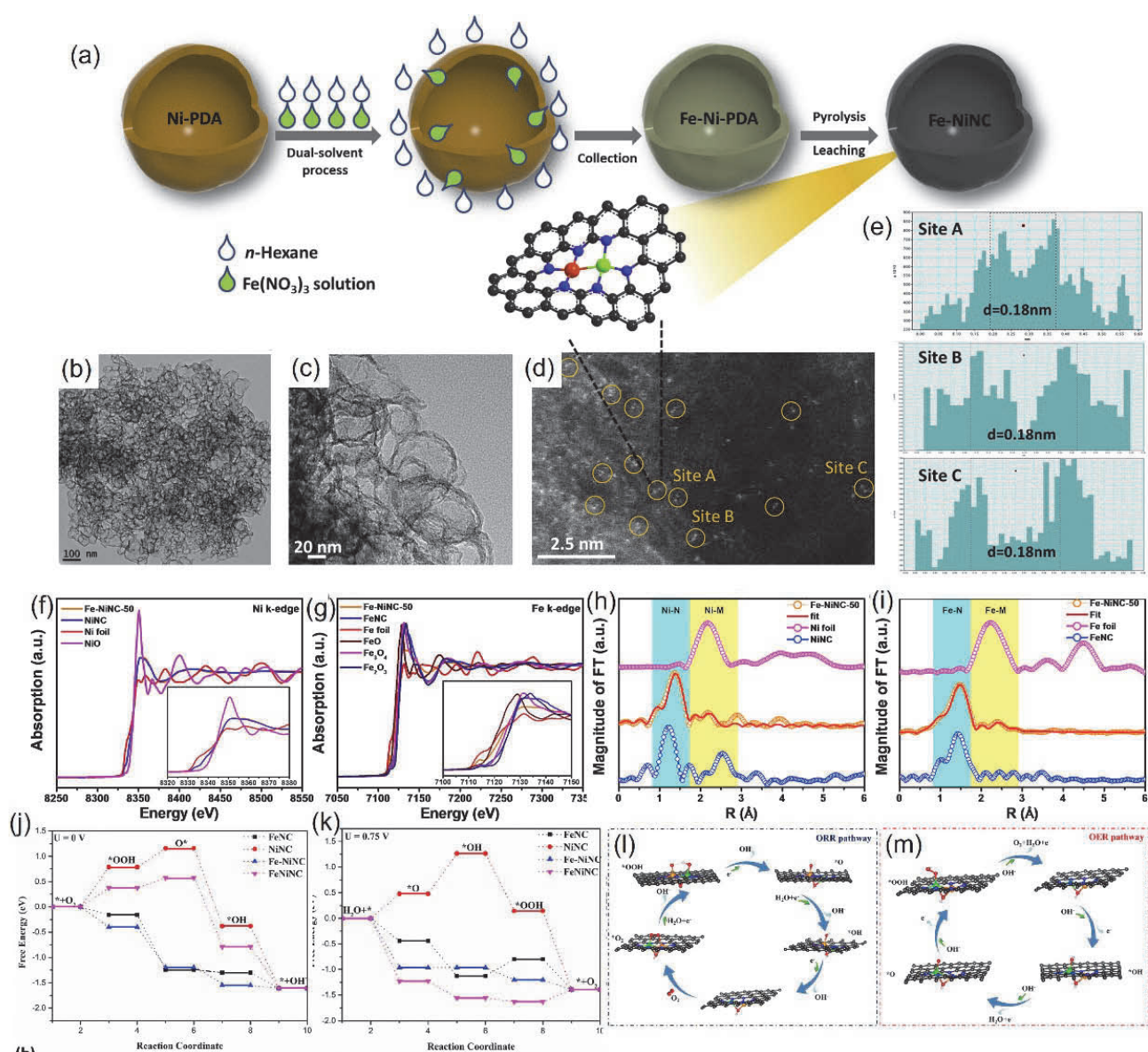


Fig. 11. (a) Schematic diagram of the synthesis of Fe-NiNC. TEM (b,c) and HAADF-STEM (d) images of Fe-NiNC. (e) The Fe-Ni distance measurements. (f,g) XANES spectra. (h,i) FT-EXAFS. Free energy diagrams (j,k) and proposed mechanisms (l,m) for ORR (j,l) and OER (k,m). (a–m) Reproduced with permission [209]. Copyright 2020, Elsevier BV.

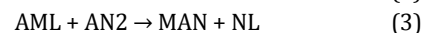
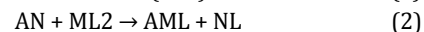
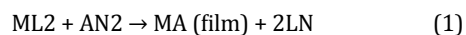
out subsequent thermal processing (Fig. 11(a)). The Fe–Ni bond not only promotes the beneficial charge redistribution around Fe and Ni sites, but also strengthens the adsorption of reactive intermediate species. In addition, the activities of Fe and Ni centers are also enhanced, so that they can catalyze ORR and OER, which offers a novel route for the preparation of multifunctional HDACs (Figs. 11(b)–(m)).

3.3. Sequential atomic layer deposition (ALD) technique

ALD is a technique to deposit materials layer by layer on the substrate as atomic film [210–212]. Its process is similar to that of normal chemical deposition. The difference is that for ALD, the previous layer plays a crucial role in the subsequent deposition reaction, resulting in only one layer of atoms being covered at a time. ALD technology was first applied to the synthesis of polycrystalline fluorescent material ZnS:Mn and amorphous Al₂O₃ insulation film by Finnish researchers. Because the process of surface chemical deposition is not only complicated but also slow, no substantial breakthrough was achieved until the mid and late 1980s. However, in the mid-1990s, due to the vigorous development of monatomic materials, people's attention to ALD technology has been greatly increased, which has been widely used in microelectronics industry. The advantages of ALD technology include excellent deposition continuity, highly uniform thickness, and ideal consistency of single-atom layers. However, the problem of slow deposition is irrelevant. The deposition film is formed by alternately pulsing the gas phase precursors, which are then chemically adsorbed and reacted on the deposited matrix [213–215]. Therefore, the selection of appropriate reaction precursor substances is very important.

It should be clarified that the surface reaction is self-limiting, that is actually the foundation of ALD. Repeated repetitions of such self-limiting process generate desired films. On the basis of different precursors and substrates, the self-limiting mechanism can be divided into two categories, namely chemisorption self-limiting (CS) and sequential self-limiting (RS). For the CS, the first precursor is imported to the matrix surface and held on it by chemisorption. After the second precursor is applied, the replacement reaction takes place, producing the corresponding by-products, until the former adsorbed on the surface is completely consumed and the reaction automatically terminates, forming the desired atom layer. While for the RS process, it is driven to form the deposited monatomic layer by the chemical reaction between precursors and matrix materials. The CS process explained by Eq. (1) consists of the direct reaction of adsorbed precursor 1 (ML2) and precursor 2 (AN2) to form a single atom layer constituted by films. As for the RS process shown in equation (2), the surface of the substrate material is first activated by the activator (AN), and then the injected precursor 1 (ML2) reacts on the surface to form the adsorption intermediate (AML), until the reaction automatically stops when the AN is completely consumed. The subsequent injection of precursor 2 (AN2) reacts with the AML to finally generate a deposited atomic layer. It should be noted that the rapid formation of a stable chemisorp-

tion layer on the matrix surface is the prerequisite of CS process. For RS process, the substrate surface is activated and the deposition process is in fact a semi-reaction combination (Eqs. (2) and (3)). The recovery characteristics and the original active state of the material surface are the main factors that distinguish the two different self-limiting reaction deposition processes.



Pt₂ dimers separated by O atoms on graphene during non-electrochemical hydrolytic dehydrogenation of ammonia borane demonstrate the reliability of ALD for the controlled synthesis of DACs [216]. So far, there have been many reports on the preparation of HDACs using ALD technology. For example, Sun *et al.* [217] synthesized Pt–Ru bimetallic monatomic pairs on NCNTs (Pt–Ru dimers/NCNTs) by a ALD process with two steps (Fig. 12(a)). During the first ALD process, the Pt precursor is easily adsorbed on N atom of the N-doped carbon material (NCNTs) as substrate material and reacts with it to form strong chemical bond and form strong metal-carrier interaction. Then, bis(ethylcyclopentadienyl) ruthenium(II) was chose as the Ru source for the second ALD process. Since Ru atoms do not attach on NCNTs efficiently in several initial cycles, they can be selectively deposited on Pt sites to successfully synthesize Pt–Ru dimers. From HAADF-STEM image with atomic resolution, this dimer can be clearly observed, and the two single atoms show obvious differences, corresponding to Pt and Ru, respectively, which can be further confirmed by XANES and EXAFS spectrograms. The dimer structure of the double monatomic sites dominated in all types, accounting for up to 70%. It is worth mentioning that with the decrease of Pt ALD process temperature, the Pt loading on the NCNTs decreases. Interestingly, under the same ALD treatment temperature, the low loading of Ru single atom on Pt–NCNT obtained at the aforementioned low temperature also decreased accordingly, which directly proves that Ru can be selectively deposited on Pt to form dimer structure (Figs. 12(b)–(j)). Furthermore, Zhang *et al.* [218] performed the synthesis of more refined bimetallic Pt/Pd monatomic materials on NCNT via the similar two-step ALD technique. Specifically, a prolonged (> 30 min) Pd ALD process was first performed to create shape-controlled Pd/NCNT support by embedding monatomic Pd sites on NCNTs with diameters from 50 to 150 nm, which effectively avoided agglomeration of the former. The final Pt/Pd SAA material was then prepared by pulsing MeCpPtMe₃ on Pd surface with octahedral configuration for two minutes at 250 °C. Moreover, Pt atoms in the material were deposited on the (100)/(111) surface of Pd species (Figs. 12(k)–(m)). It is worth mentioning that the stereoscopic configuration of the first deposited Pd single atom can be completely preserved during the subsequent second step of Pt ALD. Compared with Pd–Pt HDACs and Pt/C, Pt/Pd SAA exhibited higher catalytic activity, which is attributed to the higher density of unoccupied 5d characteristic states and lower Pt–Pt coordination number of active Pt single atoms.

In addition to the above-mentioned classical two-stage ALD

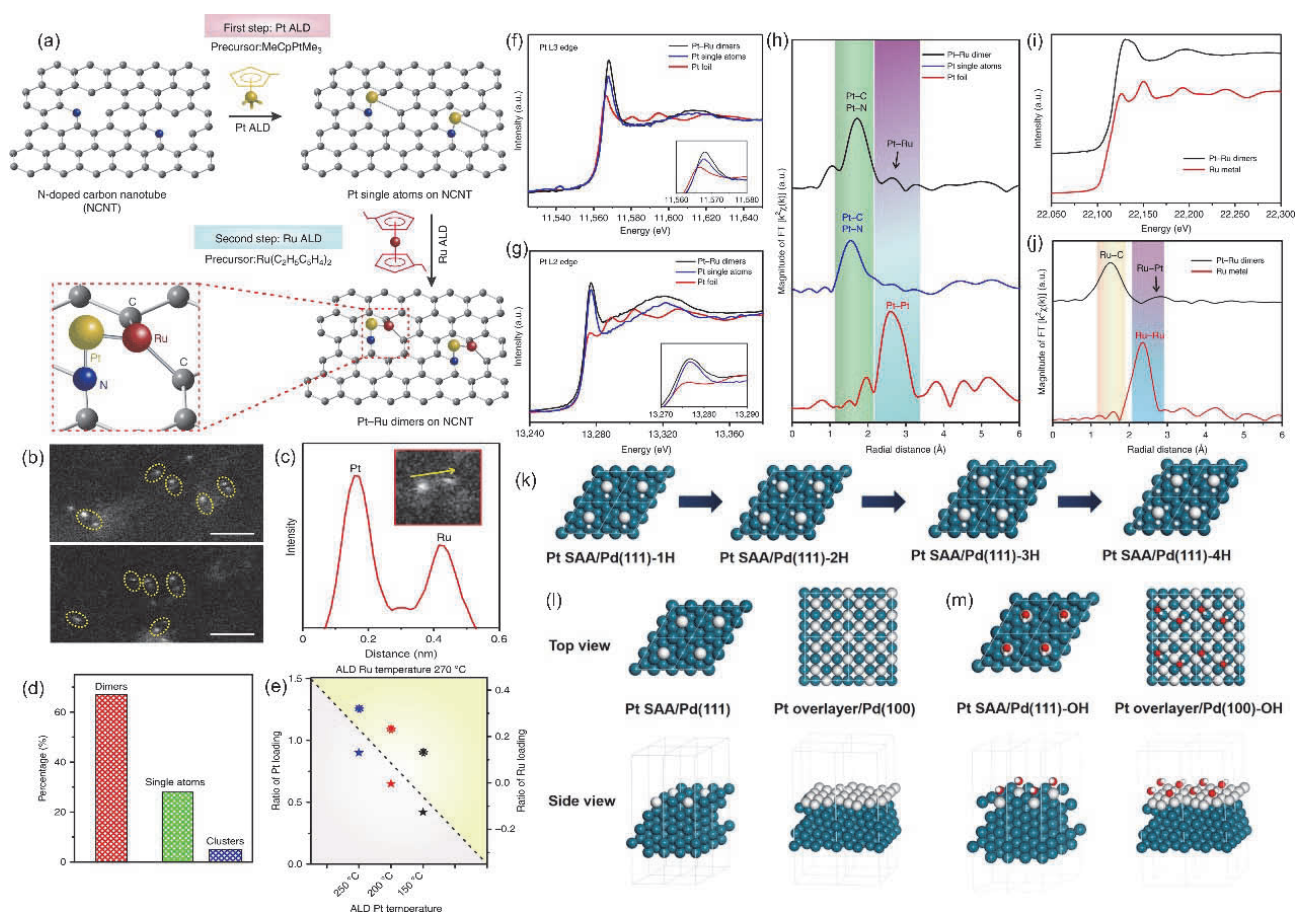


Fig. 12. (a) Synthetic illustration of Pt-Ru dimers/NCNTs using ALD technology. (b) HAADF-STEM image. (c) The intensity profile. (d) Distribution histogram of various structure types. (e) The ratio of loading Pt and Ru atoms under different ALD temperatures; XANES spectra (f,g,i) and corresponding k^2 -weighted FT-EXAFS (h,j). (k) Most stable H adsorption configurations. (l) Surface models. (m) Most stable adsorption configurations of OH. (a–j) Reproduced with permission [217]. Copyright 2019, Springer Nature. (k–m) Reproduced with permission [218]. Copyright 2019, American Chemical Society.

process for the HDAC preparation, there are also derivative ALD technologies adapted on its basis. For example, traditional ALD techniques involve generally gas-phase reactions. The undesired agglomeration of nanoparticles due to the lack of surface reaction sites is inevitable, which has been shown to be highly dependent on the surface function and the properties of deposited materials. As for the gas, this phenomenon is difficult to suppress when the substrate is extremely compatible with the deposited monatomic film, which inevitably leads to the generation of continuous films at the desired vaporization temperature, during which small clusters that do not bind strongly to the matrix aggregate to form unfavorable nanoparticles by surface diffusion. Moreover, when an excess of aqueous solvent is used for the reaction, rapid rehydroxylation of the surface occurs, preventing further embedding of the desired bimetallic monatomic pairs. For these reasons, the controlled synthesis of low-period gas phase ALD is not ideal. Luterbacher *et al.* [219] designed a brand-new kind of alternate liquid ALD technology by changing the nature of the reagent in the early stages of the deposition process, limiting the dosage of the premise and using stoichiometric amounts of precursors including triethylaluminum (TMA) to replace the purification cycle of redundant metal precursor to exclude to effectively

avoid the formation of unfavorable clusters off the surface (Fig. 13(a)). Since selective growth occurs only at target anchors, polymetallic monatomic capsules growth can be maintained or even promoted throughout the deposition process when hydroxyl carriers are used under these stoichiometric limited and mild conditions. These processes are fully substantiated by various characterizing facts. These great advantages make it easy to design the structure and composition of superior HDACs by this upgraded atomically controlled liquid phase ALD technology (Figs. 13(b) and (c)). In addition, Shen *et al.* [220] designed a gas phase ALD process under special conditions to prepare Pt-Sn bimetallic monoatomic propane dehydrogenation catalyst on Sn- and K-modified Al_2O_3 support. In the conventional ALD cycle, the nucleation and growth of monoatomic Pt species on Al_2O_3 are very slow because the initial substrate cannot initiate the self-limiting deposition reaction effectively. Their work addresses this problem by performing ALD operations in a reducing atmosphere of H_2 at 600 °C. During the H_2 -ALD operation, monolayer Pt single atoms and amorphous Pt-Sn alloy sub-nanoclusters (1 nm) containing several loosely arranged Pt atoms are easily deposited on the supported Al_2O_3 surface. H_2 -plasma may provide H atoms, radicals and other strong reducing species to effectively start the surface chemi-

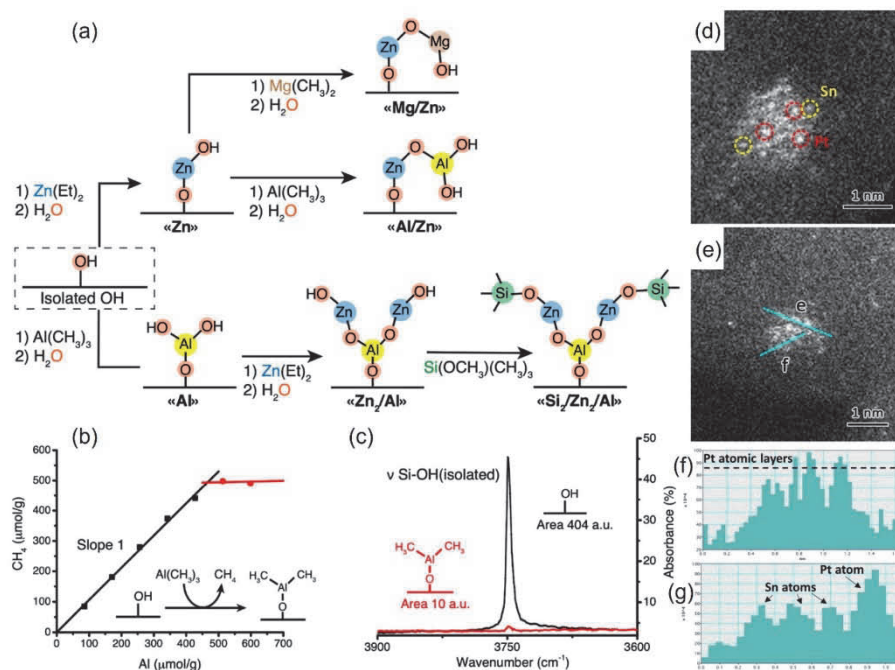


Fig. 13. (a) Synthetic illustration of various catalysts. (b) Ligand release curve during the titration. (c) DRIFTS spectra. (d,e) STEM images of Pt-Sn nanocluster. (f,g) Obvious intensity differences between Pt and Sn along the directions of the lines marked in (e). (a–c) Reproduced with permission [219]. Copyright 2022, American Chemical Society. (d–g) Reproduced with permission [220]. Copyright 2022, Wiley-VCH Verlag GmbH & CO. KGaA.

sorption reaction between Al_2O_3 and Pt precursor. Besides the atoms uniformly distributed on the Al_2O_3 surface, more Pt atoms were deposited near the metal Pt species which could induce the growth of Pt clusters. Various morphology characterization results revealed that the reduced H_2 atmosphere significantly changes the growth mode of Pt on Al_2O_3 support, and the Pt-Sn monolayer favors to expose more Pt atoms, tuning the Pt electron structure and thus activating the C–H bond (Figs. 13(d)–(g)).

3.4. Soft template self-assembly technique

The template synthesis technique is considered as a significant and extensively applied method for the fabrication of nanocomposites, in which materials with easy-to-control nanostructures and low cost are chosen as templates. The main difference between the template and ordinary preparation methods is whether the liquid or gas reactions take place in an effectively controlled region. It can be further divided into soft template and hard template methods on the basis of their characteristics and domain limiting capabilities. The former provides a dynamic equilibrium cavity, in which matter can enter and exit the cavity wall through diffusion, while the latter possesses a static hole, in which matter can only enter through the pore. Compared to the hard template method, the soft template structure is less stable, and the template efficiency is usually not satisfactory, but it is easier to both build without complex equipment and be removed during the end stage of synthesis. Compared with direct synthesis, soft template self-assembly technology has many outstanding advantages: (1) Simple synthesis and low cost. (2) It can realize the accurate

control of the morphology and properties of nanomaterials. Especially aiming to obtain specific properties, researchers can design the morphology of the target material to meet the actual needs. (3) The assembly and the dispersive stability of nanomaterials can be solved simultaneously.

These advantages make the soft template self-assembly technique highly sought after in the synthesis of HDACs. Zhu *et al.* [221] reported a soft-template oriented interlayer constrained route to synthesize Fe-Co HDAC (Fig. 14(a)). Firstly, two amphiphilic molecules, perfluorotetradecanoic acid (PFTA) and stearic acid (SA), were self-assembled into a layered micelle PFTA/SA, which was used as a two-dimensional (2D) soft template. Subsequently, $\text{Co}(\text{C}_5\text{H}_5)_2$ and $\text{Fe}(\text{C}_5\text{H}_5)_2$ metal precursors were added, and the metallic ion were adsorbed on the soft template surface due to the formation of M–O bonds, generating the FeCo-PFTA/SA. The pyrrole monomer is then coated on the layer through a hydrogen bond interaction between its NH group and the COOH group of the amphiphilic molecule. Ammonium persulfate (APS) is added to polymerize the pyrrole into the polypyrrole (Ppy) layer which is coated on the upper and lower surfaces of FeCo-PFTA/SA layer to form a three-layer sandwich structure, during which Fe/Co ions are confined by the two-dimensional soft template and the Ppy layer. Finally, independent hydrogels were obtained by hydrothermal treatment of Ppy-FeCo-PFTA/SA followed by pyrolyzing in Ar atmosphere to successfully anchor Fe/Co atoms on the N/S-doped carbon material. The appeal process and conclusions can be both confirmed by the results of various characterizations including HAADF-STEM, XANES, FT-EXAFS, etc. (Figs. 14(b)–(j)). In addition, Niu *et al.* [222] prepared CN-FeNi-P HDAC materials by using defect strategy and soft

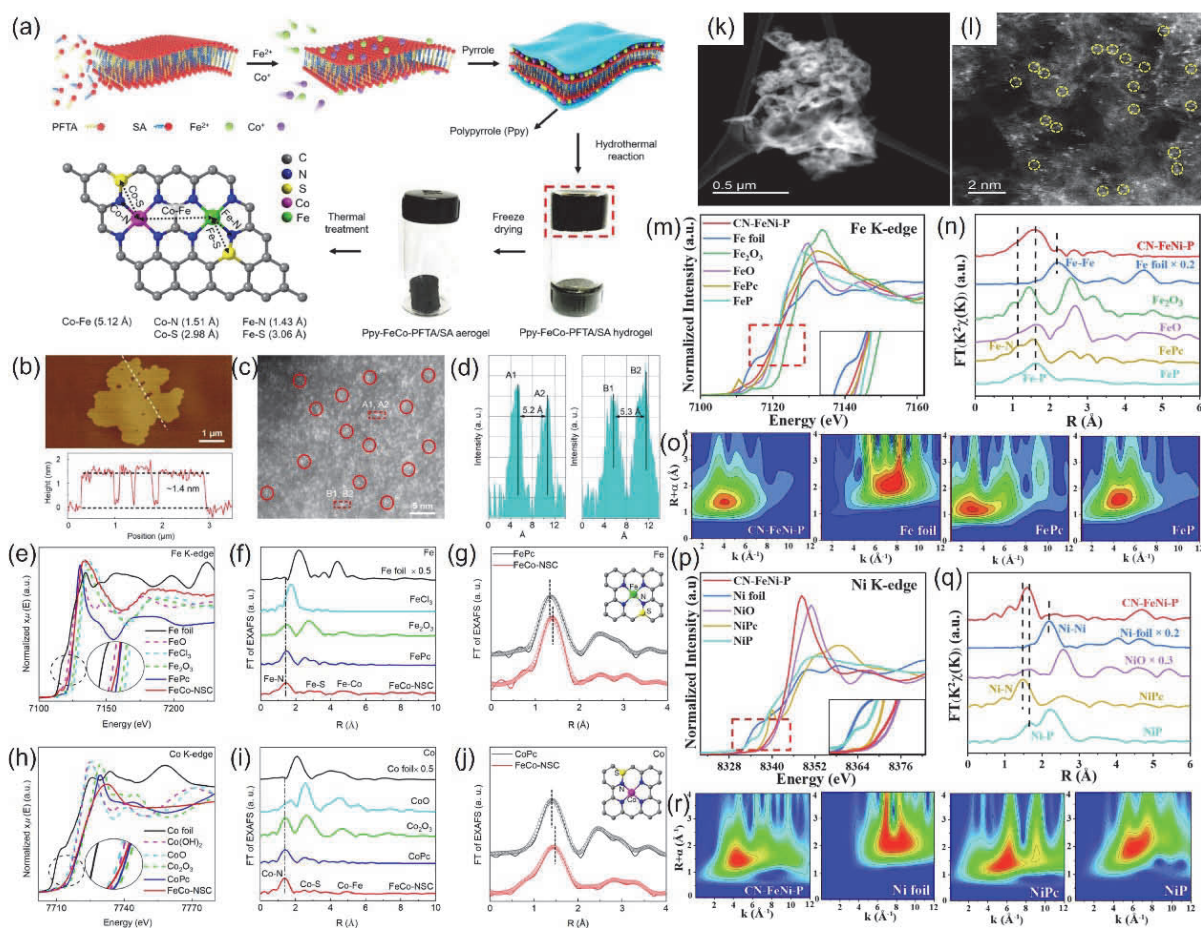


Fig. 14. (a) Synthetic illustration of FeCo-NSC. AFM image and corresponding height profile (b) and HAADF-STEM image (c). (d) The intensity plots of Fe-Co sites. (e,h) XANES spectra. FT-EXAFS spectra (f,i) and corresponding fitting in R space (g,j) of Fe K-edge (e–g) and Co K-edge (h–j) of FeCo-NSC and related samples. (k,l) HAADF-STEM images of the CN-FeNi-P. (m,p) XANES profiles. (n,q) EXAFS spectra FT k^3 -weighted in R space. (o,r) WT images of Fe K-edge (m–o) and Ni K-edge (p–r) of CN-FeNi-P and related samples. (a–j) Reproduced with permission [221]. Copyright 2022, Elsevier. (k–r) Reproduced with permission [222]. Copyright 2022, Elsevier.

template self-assembly technology, in which Fe and Ni bimetallic monatomic are bonded to N and P atoms on porous $g\text{-C}_3\text{N}_4$ substrate (CN-FeNi-P) (Figs. 14(k) and (l)). Specifically, in this study, the PH_3 -induced annealing method was used to photocatalytically degrade enoxacin (ENO) using soft template precursor. Porous $g\text{-C}_3\text{N}_4$ (CN) prepared by prepolymerization provides defect structures (N vacancies) for trapping metal monatoms. Under the action of FeNi layered double hydroxide (FeNi-LDH) and external PH_3 atmosphere (sodium hypophosphate monohydrate), the Fe active site is connected to the adjacent Ni site (Fe-P-Ni) by P bridge and obtains electrons from the latter (Figs. 14(m)–(r)), which becomes the main catalytic center. In addition, the formed Fe/Ni- N_2P_4 active sites have excellent transfer ability and utilization efficiency of electrons, which is beneficial to optimize the reaction energy barrier and electron distribution.

4. Application in tumor therapy

As mentioned in the background section, the latest statistics show that the incidence and death rates of all types of cancer continue to show a worrying trend of increasing worldwide.

Therefore, cancer is still the leading killer of human health. However, traditional surgery and chemoradiotherapy have corresponding defects. The former can only be used for local resection of early tumor tissue with clear boundary. Although the latter is a systemic treatment, it cannot achieve a precise distinction between healthy and tumor tissue, resulting in serious toxic side effects. With the rise of nanomaterials, atomic-level catalytic therapeutic strategies have attracted great interest, which can not only promote the generation of specific toxic species that can kill tumor tissue, but also do no harm to normal tissue, thus opening a brand-new world for people to treat cancer. Since few HDACs have been reported in this field, DACs anticancer materials are also introduced below.

4.1. Treatment mechanism

ROS widely refer to free radicals and non-radicals derived from O_2 , including superoxide anion (O_2^-), hydrogen peroxide (H_2O_2), hydroxyl radical (OH^\cdot), ozone (O_3) and singlet oxygen ($^1\text{O}_2$). Because they contain unpaired electrons, they have remarkable reactivity [19]. In the biology, ROS can be produced naturally in a variety of biochemical reactions in endoplasmic

reticulum, peroxisome and many other organelles. Moreover, as a natural byproduct of normal oxygen metabolism, it takes a crucial role in both homeostasis and cell signaling. Excessive ROS is eliminated by the antioxidant system under normal physiological conditions. The imbalance between oxidant and antioxidant system leads to excessive production and accumulation of ROS, which can cause mutation of intracellular mitochondrial DNA (mtDNA) and oxidative damage of lipids and proteins, and induce malignant transformation of cells and change of drug sensitivity. In addition, reactive oxygen species can also play a dual role as a signal molecule by participating in the regulation of different signal transduction pathways. On the one hand, it induces tumor cell proliferation, improves tumor cell tolerance, and promotes tumor cell metastasis; on the other hand, it induces apoptosis and even necrosis of tumor cells. This reveals that the occurrence and development of reactive oxygen species and tumor are closely linked, reactive oxygen species can be used as an important target for tumor therapy [223–226].

Related studies have shown that the stimulation of the growth or death of cells largely rests with the strength or duration of the redox signal as well as the defensive mechanism of the antioxidant. The species have opposite intracellular effects by promoting tumor proliferation or cell death. In view of these effects, different types of oxygen species with high reactivity are suitable to treat cancer cells. The new atomic-scale anticancer catalyst is on the basis of the generation of ROS or the antioxidant mechanism regulation. Targeted destruction of the latter can be achieved *in vivo* by using molecular signals to distinguish normal and cancer cells. According to different pathways that trigger ROS production in TME, anti-tumor DACs can be divided into Fenton-like reaction catalysts and other trigger pathway catalysts (Fig. 15).

The activity of various anti-tumor materials, including Fenton and Fenton-like reaction catalysts, is extremely sensitive to the tumor microenvironment (TME). However, TME exhibits adverse pH value, H_2O_2 concentration and GSH level, which have a great negative impact on catalytic reactions. Optimizing the level of TME parameters is an efficient way to increase effi-

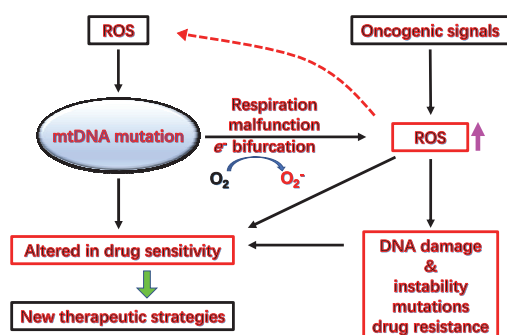


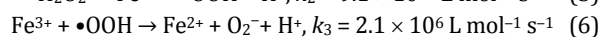
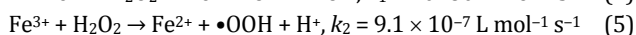
Fig. 15. Schematic diagram of biological consequences of ROS increase. Oncogenic signals in tumor cells stimulate increased ROS production. Endogenous ROS and exogenous DNA damage agents, mitochondrial mutations cause respiratory chain failure and further increase ROS production. The above fault may affect the apoptotic response to anticancer drugs, making cancer cells resistant to the drugs. A surge in cellular ROS causes DNA damage and promotes mutations, which in turn leads to increased drug sensitivity.

cacy. Specifically, Fenton and Fenton-like reactions must satisfy three conditions to generate sufficient target ROS species. (1) It needs to produce sufficient H_2O_2 concentration. Although the concentration of H_2O_2 in TME is $100 \mu\text{mol L}^{-1}$, which is more than 5 times higher than that of normal cells, this concentration is still not sufficient to continuously generate abundant ROS species to achieve the ideal effect of cancer treatment. Adding exogenous H_2O_2 , metal peroxides and other chemical reagents can directly/indirectly increase the concentration of endogenous H_2O_2 . (2) The generation rate of ROS species such as $\bullet\text{OH}$ must be fast enough to minimize the time of strong oxidation of cancer cells, thereby avoiding the reactivation of tumor tissue. This can be achieved by adjusting the pH of the TME. In 1956, Warburg *et al.* [227] found that most tumor cells had defects in oxidative phosphorylation and related enzyme expression. Compared with normal cells, tumor cells require large amounts of glucose for anaerobic glycolysis to meet their own rapid proliferation needs. Even in the presence of sufficient oxygen, tumor cells acquire energy primarily through anaerobic glycolysis, accompanied by the production of numerous intermediate metabolites. In this process, a large amount of lactate and carbonic acid is produced, which accumulates in the extracellular matrix of the tumor, resulting in a pH of approximately 7.4 for normal tissue and blood, while the pH of tumor tissue is commonly less than 6.5 and some only 5–6. However, the optimal pH region of the Fenton reaction is 2–4, resulting in the TME pH value that is already weakly acidic remains to be further reduced. To solve this problem, the common method is to introduce exogenous acid, but its application dose is difficult to control. The efficiency of CDT mediated by Fenton reaction mainly depends on Fe^{2+} . However, under the pH condition of TME, iron ions will precipitate rapidly into inactive $\text{Fe}(\text{OH})_x$ sediment, and Fe^{2+} will slowly convert into inert Fe^{3+} . Therefore, preventing the adverse conversion of iron ions to overcome the excessive dependence of Fenton catalysts on the acidic environment has a wider application prospect and will be the research frontier in the future. (3) The generated ROS species need to directly attack tumor cells as greatly as possible, rather than damaging the reaction with the main reducing species glutathione (GSH), which is a tripeptide formed by glutamic acid, cysteine and glycine, and plays the antioxidant role in TME. It will reduce free radicals into acidic substances to reduce its toxic side effects on normal cells. However, GSH is generally overexpressed in TME, which leads to a decrease in target ROS level. Therefore, reducing the concentration of GSH in TME has been proven as a feasible method to enhance the catalytic activity of Fenton/Fenton-like catalysts.

4.2. Fenton-like reaction catalysts

According to the different sources of substances that trigger ROS production in TME, the current anticancer catalysts can be divided into endogenous and exogenous pathways. So far atomic catalytic materials mainly play a role through the former. The endogenous reactions triggered by DACs are mainly based on Fenton and Fenton-like reactions in tumors, which are called chemodynamic therapy (CDT) [228–230]. Specific-

ly, through these reactions in the presence of divalent iron ions, H_2O_2 in TME is mainly converted into highly toxic hydroxyl radicals (OH^\cdot) and secondary peroxy radicals (O_2^\cdot) without additional external action, which is a new strategy for effective regulation of tumor microenvironment to achieve tumor therapy (Eqs. (4–6)). The step of Eq. (5) determines the overall Fenton reactive rate because of its relatively low constant k_2 . Hence, for the application, abundant Fe^{2+} is needed to supply the reactive system to ensure that sufficient OH^\cdot is produced. However, the continuous accumulation of a mass of Fe^{3+} results in the production of a large amount of iron sludge, which causes catalyst poisoning. In addition, although the concentration of hydrogen peroxide in the tumor microenvironment is usually higher than that in normal tissues, it is not sufficient to support the continuous production of sufficient amounts of $\cdot\text{OH}$ to kill tumor tissue. Therefore, in vitro delivery of additional H_2O_2 or Fenton reaction catalysts has become a solution to this problem, but the off-target of the delivery medium and the toxicity caused by a large number of catalysts often lead to inefficient treatment and serious side effects. Therefore, the design of Fenton reaction catalysts with remarkable catalytic efficiency and biocompatibility from the source has become a potential solution. Recently, lots of studies have found that in addition to Fe^{2+} and Fe^{3+} (Eqs. (4–6)), other metal ions, such as Mn^{2+} , Cu^{2+} , Pd^{2+} and other atomic-level catalytic centers can be used as catalysts to endogenously trigger Fenton or Fenton-like reactions in tumors [231–234].



Although Fenton reaction has been applied to treat the can-

cer in recent years, the unsatisfactory conversion of Fe^{3+} to Fe^{2+} and the slow reaction kinetics greatly limit the therapeutic effect of Fenton reaction. In this regard, Shi's team constructed a 2D bimetallic monoatomic catalyst to solve the kinetic bottleneck of Fenton reaction by loading atomically dispersed Fe onto MoS_2 nanosheets as a carrier ($\text{MoS}_2@\text{SA-Fe}$), and generated abundant OH^\cdot through H_2O_2 to oxidize tumors and thus deplete them [235]. Specifically, the preparation of $\text{MoS}_2@\text{SA-Fe}$ is on the basis of a sophisticated one-step hydrothermal synthesis method to obtain $\text{MoS}_2@\text{SA-Fe}$ nanoflowers, and then ultrasonic treatment is performed to customize the two-dimensional nanostructures. Finally, the morphology of the nanosheets is further modified by amine-PEG ($\text{NH}_2\text{-PEG}$) to obtain the final product $\text{MoS}_2@\text{SA-Fe-PEG}$ (MSFP). In addition, they also prepared pure MoS_2 nanoflowers with similar microscopic morphology in the absence of iron source for comparison ($\text{MoS}_2\text{-PEG}$). Compared with the sample containing only a single Mo metal element and other traditional nano-anticancer catalysts, the catalytic anti-cancer efficiency of the constructed MSFP nanosheets was greatly improved, with satisfactory biological safety and therapeutic effect. Moreover, the co-catalytic mechanism of bimetallic monoatomic nanocatalysts has been systematically proved. Both cell experiments and in vivo results show that MSFP nanosheets have high peroxidase-like activity ($V_{\text{max}} = 4.37 \times 10^{-8} \text{ L mol}^{-1} \text{ s}^{-1}$, $K_m = 15.06 \mu\text{mol L}^{-1}$) (Figs. 16(a)–(d)). The superior performance mainly comes from the following points. Doping Fe atoms in MoS_2 nanocrystals not only forms abundant Fenton reactive Fe sites, but also facilitates the generation of S vacancy defects in the plane and edge of the nanosheets, which greatly promotes the process of H_2O_2 capturing electrons to promote the generation of OH^\cdot . In addi-

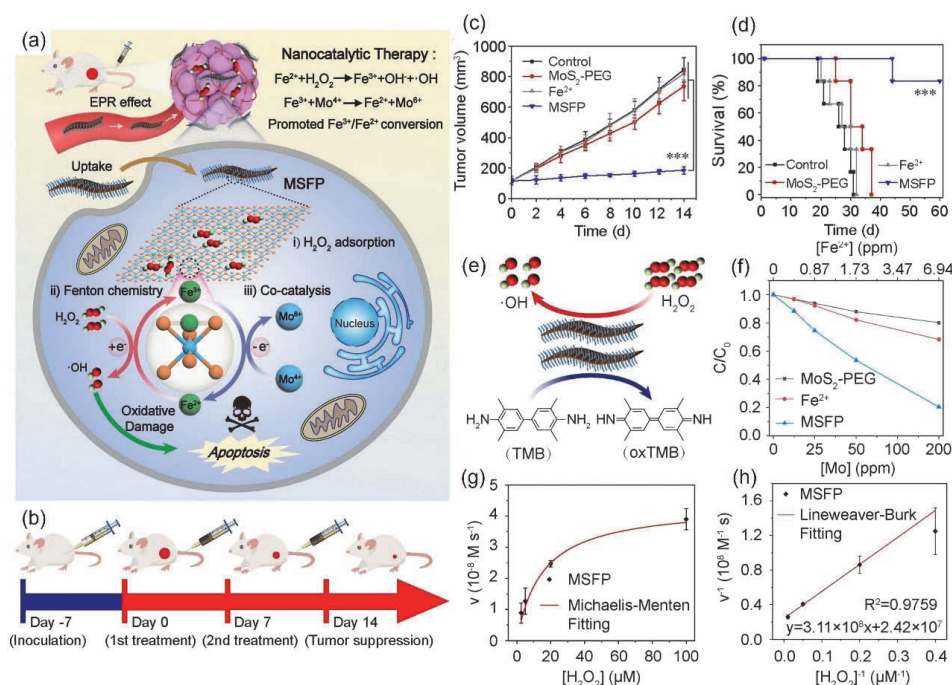


Fig. 16. Schematic diagrams of the mechanism of endogenous Fenton response triggered by MSFP (a) and follow-up anti-tumor therapy for MSFP (b). Growth (c) and survival curves (d) of mice 4T1 tumor. (e) Schematic diagram of MSFP catalyzing the formation of $\cdot\text{OH}$, resulting in the oxidation of TMB (colorless) to oxTMB (blue). (f) Normalized absorbance of MB (C/C_0) after 30 min in acidic PBS containing $100 \mu\text{M H}_2\text{O}_2$. (g) Michaelis-Menten dynamics. (h) Line Weaver-Burk plotting of MSFP. (a–h) Reproduced with permission [235]. Copyright 2022, John Wiley and Sons Ltd.

tion, numerous Mo⁴⁺ sites are exposed on MoS₂ support, which is helpful to weaken the slow kinetics limit and lead more Fe elements exist in the form of Fe²⁺, thus providing continuous power for efficient Fenton (Figs 16(e)–(h)).

Furthermore, Zhao et al. [16] embedded atomic-level Fe and Co elements on NC to generate bimetallic non-alloyed atom pairs (FeCo-DIA/NC). Subsequently, hyaluronic acid (HA) was coated on the surface to achieve precise targeting of tumor tissues (FeCo-DIA/NC@HA). Specifically, the whole preparation process can be divided into four steps. Firstly, the Fe and Co atoms provided by Fe(acac)₃, Fe(III) acetylacetonate and Co(NO₃)₂ precursors were spaced in zeolite imidazolate frame-8 (ZIF-8) material with appropriate nanocavities to form tri-metal FeCoZIF-8. Secondly, the surface of FeCoZIF-8 was covered with a protective silicon oxide shell (FeCoZIF-8@SiO_x) to effectively prevent irreversible melting and aggregation during succeeding pyrolysis. After that, isolated FeCo atoms

were successfully inserted on the NC by conventional pyrolysis in Ar atmosphere. During the calcination process, both SiO₂ shell and FeCoZIF-8 inner core maintained their original morphology without any aggregation. Using acid to remove the SiO₂ and metal oxide nanoparticles, the final FeCo-DIA/NC was obtained. It is worth mentioning that without any external energy input, the two atomic-level metal active sites Fe-N₄ and Co-N₅ in the material can achieve parallel catalysis with a clear division of labor. The former is mainly for the Fenton reaction and catalyzes H₂O₂ and O₂ concurrently to generate OH⁻ and O₂⁻, while the latter is responsible for the Fenton-like reaction and catalyzes the same reactants to form singlet ¹O₂ and O₂⁻, that can simultaneously achieve efficient triggering of the Fenton/Fenton-like reaction. In addition, the desired synergy between bimetallic single atoms can reversely convert the toxic ROS species (OH⁻, O₂⁻, and ¹O₂) produced by the appeal catalysis into H₂O₂ in acidic TME, resulting in a surprisingly efficient

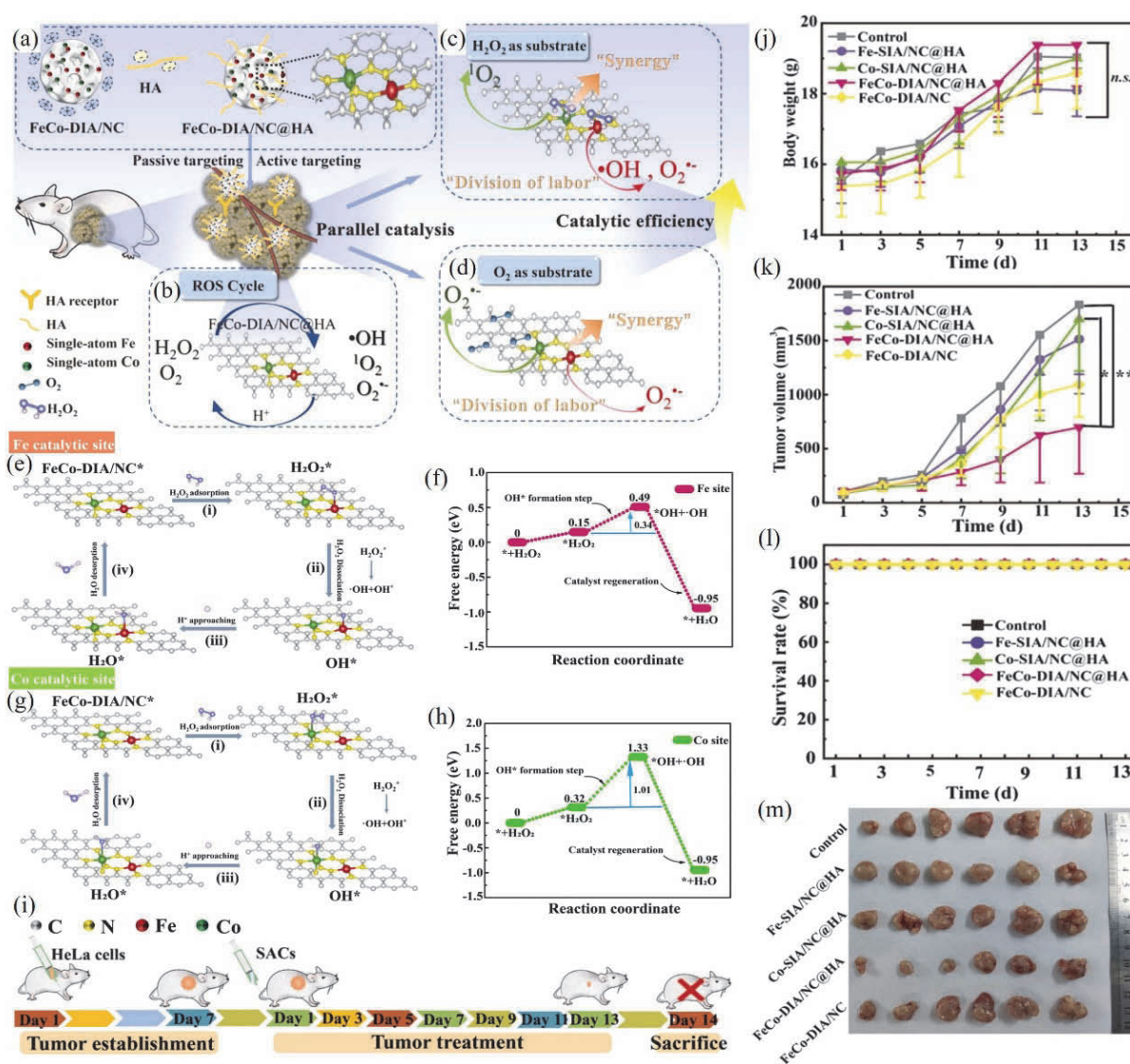


Fig. 17. (a–d) Schematic diagram of the synergistic and “division of labor” catalytic mechanisms of FeCo-DIA/NC for “ROS cycling” and concurrent catalytic therapy in tumors. (e–h) DFT simulations of Fenton activity. Proposed reaction mechanisms at the Fe (e) and Co (g) sites. Free energy diagrams of Fenton process at Fe (f) and Co (h) sites. (i) Schematic diagram of in vivo studies. Body weight curve (j), tumor tissue proliferation curve (k) and survival rate (l) of mice during treatments. (m) Digital photographs of the dissected tumor. Reproduced with permission [16]. Copyright 2022, Elsevier.

anti-tumor “ROS cycle” (Figs. 17(a)–(h)). These unique characteristics make the catalytic activity of FeCo-DIA/NC for Fenton and Fenton-like reactions significantly superior to that of Fe-SIA/NC and Co-SIA/NC catalysts with corresponding monometallic atomic sites dispersed on the same substrate material. They also prepared control samples of two SACs, Fe-SIA/NC@HA and Co-SIA/NC@HA, by the same synthesis procedure. The mice that established the HeLa model were classified and given the synthetic HDAC and SAC agents for *in vivo* treatment comparison experiments. As expected, tumor growth was significantly inhibited in mice treated with FeCo-DIA. Although Fe SIA/NC@HA and Co SIA/NC@HA also show some anti-tumor effect, it is far less pronounced than HDAC. The well-dispersed FeCo bimetallic reactive sites can efficiently target tumor tissues and catalyze H_2O_2 to form ROS, thereby significantly reducing tumor volume (Figs. 17(i)–(m)). *Vitro/vivo* experiment results verify that this material can significantly reduce cell viability and inhibit the growth of cancerous tissues through the novel “ROS cycle” pathway, which can achieve satisfactory therapeutic effects at extremely low metal concentrations, highlighting its broad clinical application potential.

Furthermore, Zheng *et al.* [236] fabricated atomically dispersed Fe/Pt HDAC ((Fe, Pt)_{SA}-N-C) in a controllable way via a secondary doping strategy. The successful preparation of

atomically heterogeneous Fe/Pt active sites can be verified by related characterization techniques. The spacing between active monatomic Fe₁ (Fe-N₃) and Pt₁ (Pt-N₄) sites can be achieved to a relatively accurate 2.38 Å (Figs. 18(a)–(c)). The preparation process is that the atomically dispersed Fe pre-catalyst (Fe_{SA}-N-C) was firstly prepared by “isolation and pyrolysis”. Specifically, Fe(acac)₃ is typically spaced in ZIF-8, then subsequently freeze-dried and pyrolyzed. Secondly, the mixture of H₂PtCl₆, cyanoguanidine and Fe_{SA}-N-C was similarly lyophilized and pyrolyzed through a secondary doping treatment to introduce uniformly dispersed Pt atomic sites. As a control, an atomic catalyst (Fe_{SA}-N-C) was prepared through a similar primary doping process. As for (Fe, Pt)_{SA}-N-C, it possesses a synergistic effect between heteronuclear metal monatomic sites, which is conducive to catalyzing Fenton-like reactions, exhibiting a doubling of antitumor therapeutic effect compared with Fe_{SA}-N-C. To expand, Fe-N₃ group, due to its beneficial electronic structure, geometric morphology and sufficient active sites, can effectively activate Fenton-like reaction, release abundant toxic hydroxyl radicals in tumor tissues, thus effectively induce apoptosis of tumor cells. DFT calculations revealed that Pt-N₄ group can further increase the overall Fenton-like catalytic activity of (Fe, Pt)_{SA}-N-C up to 128.8% by optimizing the deployment of the 3D electron orbital of Fe-N₃ single atomic site. Surprisingly, amorphous carbon can demon-

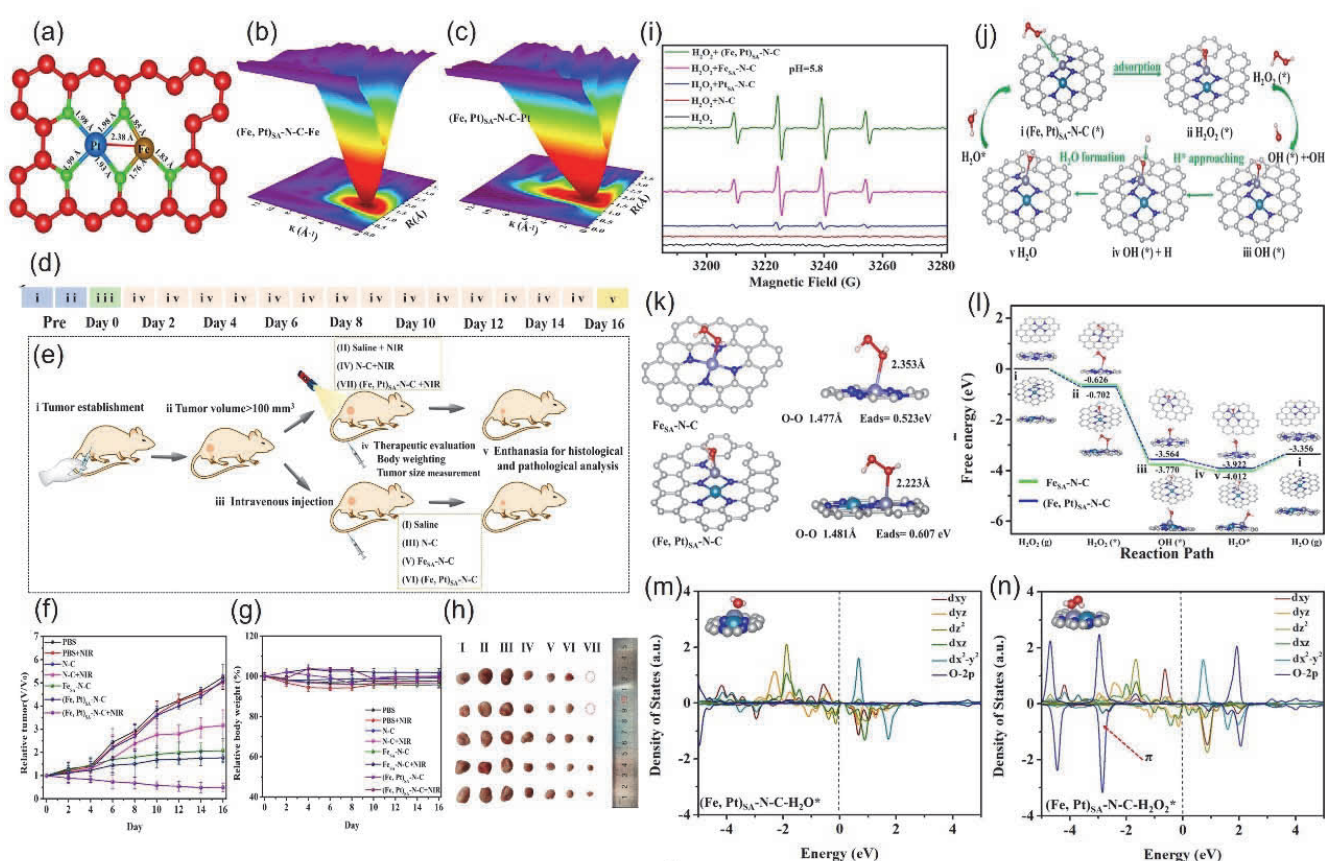


Fig. 18. (a) The structure of (Fe, Pt)_{SA}-N-C. (b) Fe K-edge EXAFS. (c) Pt L₃-edge EXAFS. (d,e) *In vivo* treatment options. Tumor growth curves (f), weight change curves (g), Photos (h) of corresponding tumor tissue. (i) ESR spectra of BMPO/•OH. (j) Probable Fenton-like reaction mechanisms for attaining •OH on (Fe,Pt)_{SA}-N-C. (k) H₂O₂ adsorption models. (l) Free energy diagrams for Fenton-like reaction. Projected density of states of (Fe, Pt)_{SA}-N-C after adsorbing H₂O* (m) and H₂O₂* (n). Reproduced with permission [236]. Copyright 2022, American Chemical Society.

strate ultra-high photothermal conversion efficiency under 808 nm laser irradiation, which makes it more ideal to enhance the effect of tumor treatment (Figs. 18(d)–(n)).

4.3. Other trigger pathway catalysts

In addition to the appeal of the CDT pathway that triggers the mass production of ROS with anticancer potency by catalyzing Fenton and Fenton-like reactions, sonodynamic therapy (SDT) can also efficiently achieve the same goal, which has aroused great research enthusiasm. Its anticancer mechanism is mainly interpreted as the singlet oxygen (negative ion molecular oxygen with strong oxidizing ability in the excited state) mechanism. Its action process is as follows: after ultrasonic treatment, the sound-sensitive substances (such as hematoporphyrin) stored in tumor cells absorb energy and undergo electronic transition to high energy status. When back to the low energy status, a large amount of energy is released, that stimulates hematoporphyrin to produce extremely unstable trivalent hematoporphyrin which quickly splits into monovalent hematoporphyrin, releasing O-based ROS. SDT uses ultrasound to have a strong ability to penetrate biological tissues [237–239]. In particular, focused ultrasound can non-invasively

focus sound energy on deep tissues to activate some sound-sensitive catalysts to finally trigger the formation of ROS, which provides a potential localization treatment method to reduce the risk of side effects in other parts of the body. So far, although bimetallic single atom catalysts applied to the field of cancer treatment through the SDT pathway has not been reported yet, it is worth drawing on. Wu *et al.* [240] reported an ultrasound (US) activated SACs for sonodynamic therapy of osteomyelitis infected with methicillin resistant staphylococcus aureus (MRSA) (Fig. 19(a)). Since osteomyelitis infection is stubborn and located deep in the bone tissue, the SDT approach is well-suited for its treatment. They chose zirconium-based porphyrin metal organic framework (HNTM) as the substrate, which can enhance the overall stability. After that, Pt atoms with strong capacity of both electron capture and oxygen adsorption were embedded in HNTM (HNTM-Pt), which significantly enhanced the sonocatalytic ability of the sonosensitizer. The gold nanorods (Au NRs) are then loaded on the HNTM-Pt (HNTM-Pt@Au) as actuators for US response, which can increase the system's absorption of ultrasonic energy by increasing ultrasonic cavitation. In addition, Au and Pt single atoms can be used as electron acceptors to accelerate the electron transfer and the electron-hole separation efficiency to

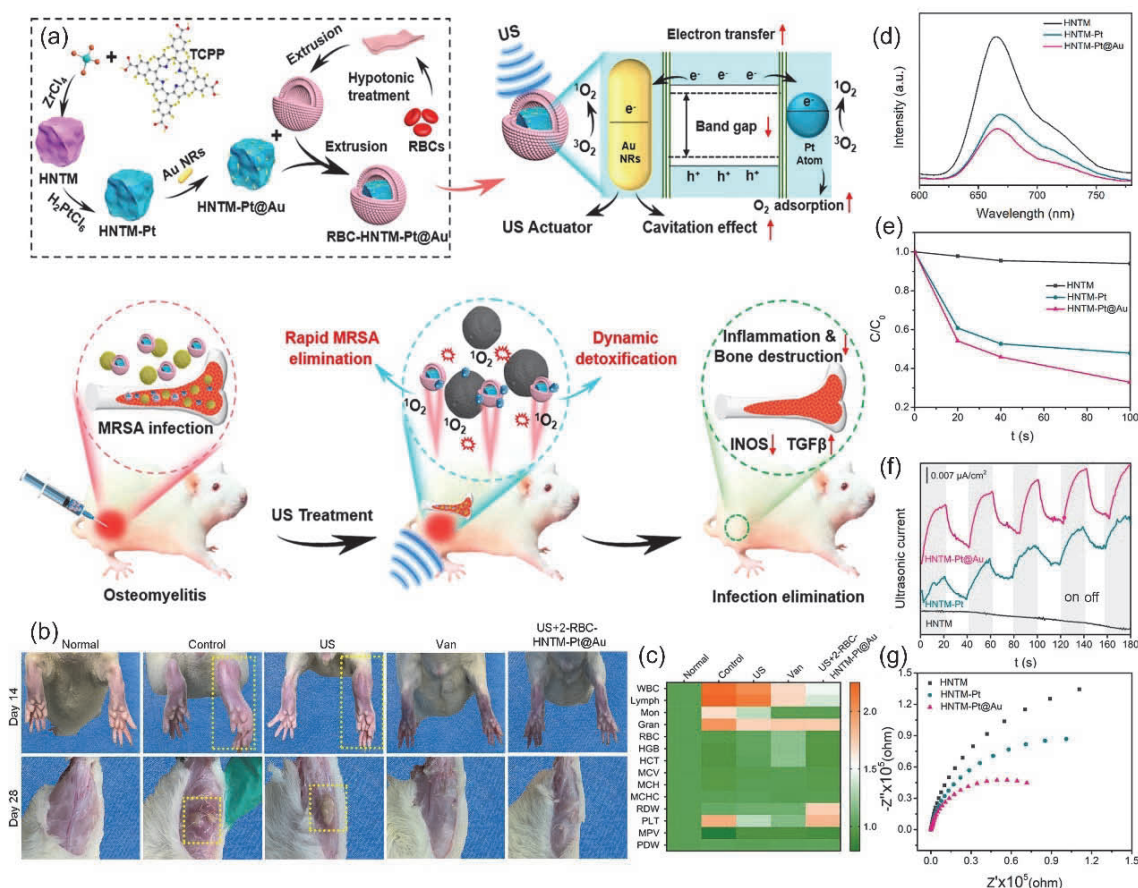


Fig. 19. (a) Schematic diagram of the synthesis of RBC-HNTM-Pt@Au and the efficient treatment of osteomyelitis via SDT mechanism. (b) Photos of the rat surgical site. (c) Routine blood tests after 4 weeks of treatment ($n = 3$). (d) Photoluminescence spectra. (e) The ¹O₂ comparison curve detected by 1,3-diphenylisobenzofuran (DPBF) degradation. (f) Ultrasonic current test. (g) Electrochemical impedance spectra. Reproduced with permission [240]. Copyright 2021, American Chemical Society.

enhance SDT performance. Finally, HNTM-Pt@Au was coated on rat red blood cell (RBC) membrane to obtain superior biocompatibility and toxin neutralization ability. The final synthesized RBC-HNTM-Pt@Au material exhibits outstanding antibacterial properties with the inhibition efficiency of MRSA up to 99.9% under 15 min of US irradiation. Furthermore, RBC-HNTM-Pt@Au can propel directionally under the guidance of US, thus having the ability to dynamically neutralize secreted toxins (Figs. 19(b)–(g)). This work has stimulated further research on the development of DACs as potent sonosensitizers for the SDT pathway.

Since Zn^{2+} can promote osteogenic differentiation of osteoblasts, Cao et al. chose porphyrin-based SAC ($g\text{-ZnN}_4$) with good biocompatibility, then doped MoS_2 ($g\text{-ZnN}_4\text{-MoS}_2$) on its surface to construct single-atom sonosensitizers with heterogeneous interfaces to similarly treat MRSA-infected osteomyelitis via the SDT pathway (Fig. 20(a)) [241]. The heterogeneous Zn/Mo bimetallic monoatomic material not only has abundant charge transfer channels to enhance the overall electron transfer efficiency of the sonosensitizer after receiving US irradiation and the separation efficiency of the photogenerated charge carrier, causing an increased transfer rate of interfacial charge to adsorbed O_2 . In addition, DFT calculations demonstrated that $g\text{-ZnN}_4\text{-MoS}_2$ exhibits sufficient reactive sites, resulting in a significantly reduced O_2 activation energy, which can increase the production of active species 1O_2 . $g\text{-ZnN}_4\text{-MoS}_2$ with the ability to effectively kill MRSA with superior biodynamic therapy,

can also promote osteogenesis by continuously releasing Zn^{2+} from fixed Zn single atoms, serving as an adjuvant therapy that significantly inhibits inflammation and estimates erosion (Figs. 20(b)–(k)).

Platinum-based anticancer agents have played a central role in the current cancer treatment and have shown promising therapeutic outcomes since cisplatin which is a platinum metal complex ($cis\text{-[PtCl}_2(\text{NH}_3)_2]$) was approved for clinical use in 1978 [242]. It targets DNA and interferes with the replication of DNA in cells or binds nuclear and cytosolic proteins by catalyzing the release of ROS, so as to play a broad spectrum and potent anti-cancer effect. It is one of the most commonly used drugs in chemotherapy. However, due to the lack of selectivity and renal excretion of cisplatin, its serious adverse reactions seriously affect its clinical efficacy. In addition, some tumors are not sensitive to cisplatin per se (e.g., colorectal, lung, and breast cancers), while others may become resistant to cisplatin after a treatment cycle (e.g., ovarian cancer). Massive efforts have been made to develop novel catalysts to overcome the defects of drug resistance and toxic side effects of conventional cisplatin [243]. For example, ruthenium complexes with similar structures have been shown to be effective alternative drugs for cisplatin, exhibiting three promising properties in medical applications: (1) adequate ligand exchange rates, (2) various available oxidation states, and (3) facilities for mimicking iron binding to a variety of biomolecules. However, many ruthenium organometal complexes have ultra-low water solubility and

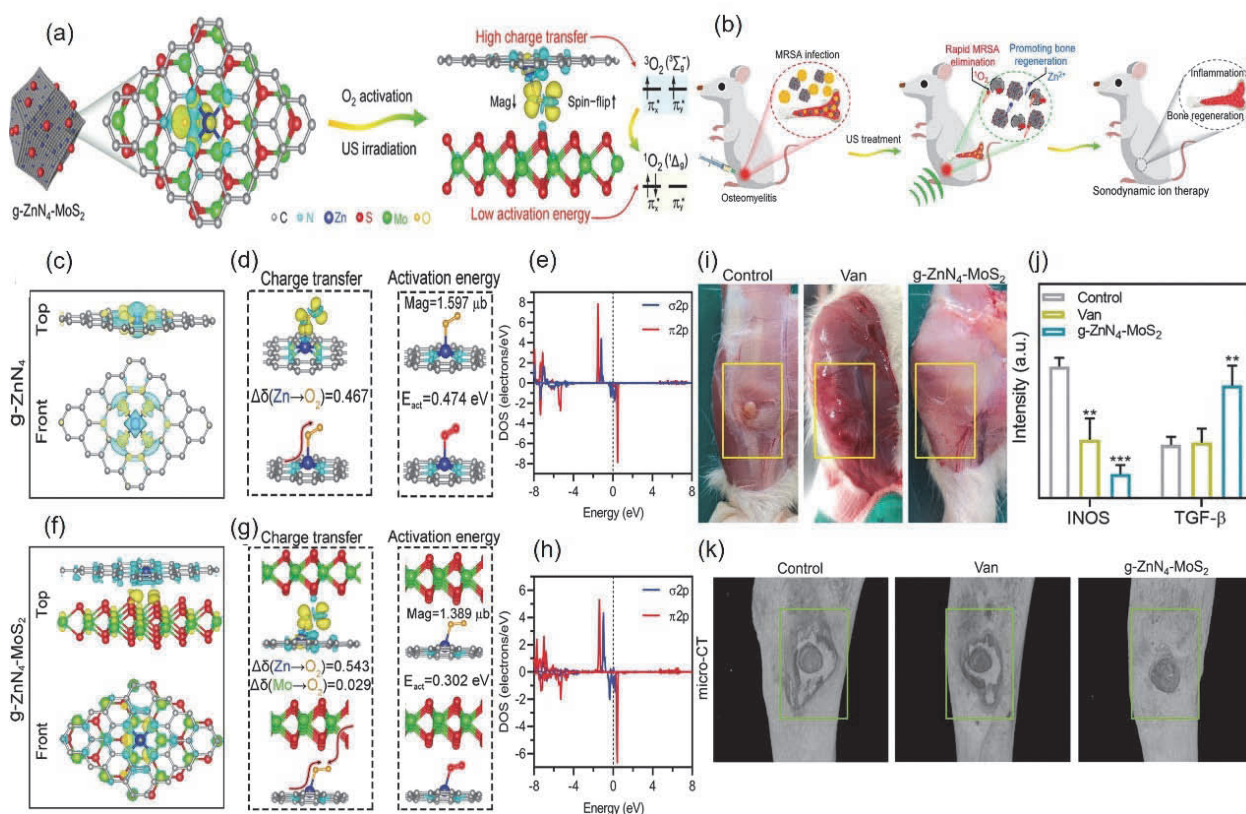


Fig. 20. Schematic diagrams of sonocatalytic mechanism (a) and osteomyelitis operation via sonodynamic therapy (b). Charge density difference (c,f) of $g\text{-ZnN}_4$, band charge, O_2 activated energy, magnetic moment (d,g), and DOS (e,h) of $g\text{-ZnN}_4$ (c–e) and $g\text{-ZnN}_4\text{-MoS}_2$ (f–h). (i) The infected leg wound. (j) Fluorescence intensity statistics of inducible nitric oxide synthase and transforming growth factor- β . (k) Micro-CT analysis of infected legs. Reproduced with permission [241]. Copyright 2022, Wiley-VCH Verlag.

stability, limiting their use as antiproliferators. This drawback was found to be effectively addressed by the addition of dialkane sulfoxide derivatives. For example, Dyson *et al.* [244] successfully synthesized a Ru-based material, which showed remarkable anti-proliferation activity against the cisplatin resistant/non-resistant tumor tissues. Inspired by these, Romero *et al.* [245] first synthesized monometallic complexes $[\text{Ru}(\eta^6\text{-C}_{10}\text{H}_{14})(\text{Cl}_2)(\text{HdmoPTA})](\text{OSO}_2\text{CF}_3)$ (1), $[\text{Ru}(\eta^6\text{-C}_{10}\text{H}_{14})(\text{Cl}_2)(\text{dmoPTA})]$ (2), and then synthesized diheterometallic monoatomic Ru-M complexes $[\text{Ru}(\eta^6\text{-C}_{10}\text{H}_{14})(\text{Cl}_2)\text{-}\mu\text{-dmoPTA-1}\kappa\text{P:2}\kappa^2\text{N,N'-MCl}_2]$ (M: Zn (3), Co (4), Ni (5), dmoPTA: 3,7-dimethyl-1,3,7-triaza-5-phosphabicyclo[3.3.1]nonane) by reacting the deprotonated complex (2) with the corresponding MCl_2 salt in anhydrous MeOH (Fig. 21(a)). The antiproliferative activities of the complexes against Caco-2/TC7 colon cancer cells were examined by MTT assay. It was found that the pure Ru-based materials (1) and (2) showed almost no activation, while the activities of the bimetallic SACs (3) (IC_{50} : $9.07 \pm 0.27 \mu\text{mol L}^{-1}$), (4) (IC_{50} : $5.40 \pm 0.19 \mu\text{mol L}^{-1}$) and (5) (IC_{50} : $7.15 \pm 0.30 \mu\text{mol L}^{-1}$) were significantly higher than that of cisplatin ($\text{IC}_{50} = 45.6 \pm 8.08 \mu\text{mol L}^{-1}$) (Figs. 21(b) and (c)). Although they have great antiproliferative activity, there is no observable viability decrease in healthy cells during the treatment. The information of the possible mechanisms of these complexes was obtained by cell cycle, ROS and gene expression studies. It can be found that the feature of the second metallic atom coor-

ordinated with dmoPTA ligand determines the apoptosis mechanism activated by the complex, which makes these bimetallic complexes have different anti-tumor mechanisms. For example, the growth of tumor cells can be restrained by samples (3) and (4) through stopping the G2/M phase of the cell cycle and by consuming the G0/G1 cell population, respectively. Their work gives inspiration to the development of new bi/multi-heterometallic antitumor SACs.

4. Conclusions and perspectives

The HDACs have many fascinating advantages, such as ultra-high selectivity and specific activity and 100% atomic utilization efficiency, making them the frontiers of many research fields in recent years. Different from other common nano-scale and single-atom catalysts, there are interactions between two heterogeneous metal sites in DACs, which significantly reduces the reaction energy barrier and promotes the catalytic process. With the further research, the controllable preparation of DACs is becoming simpler and simpler while the catalytic activity is getting higher and higher. In the field of nano-catalytic medicine such as tumor therapy, DACs have shown surprisingly ideal performances, breaking through the problems of high cost and side effects of traditional therapies, thus becoming a rising star light in competition. We comprehensively summarize the latest progress about DACs such as characterization technolo-

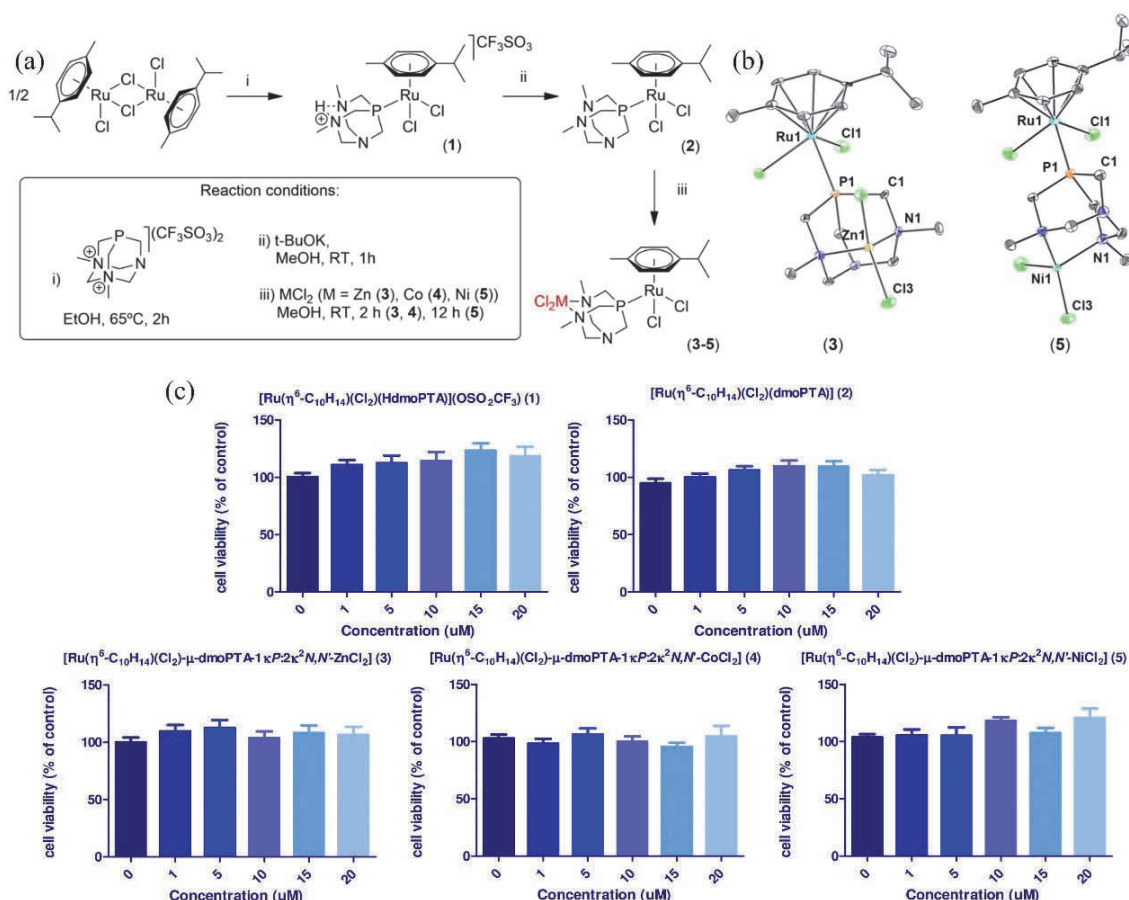


Fig. 21. Schematic diagrams of the synthesis of samples (1–5) (a) and crystal structures of samples (3) and (5) (b). (c) Viability of normal Caco-2 cells treated with samples 1–5 for 72 h after 15 d of inoculation ($n \geq 12$). Reproduced with permission [245]. Copyright 2022, MDPI AG.

gies, synthesis methods and applications in anti-cancer nanomedicine. Although fruitful results have been achieved on these factors so far, it must be admitted that the research of dual-metal atom catalysts is still in its infancy, and there are various potential bottlenecks that still hinder large-scale practical applications.

(1) The main challenge is that the atomic metal loading in HDACs reported so far is still low. Once the load of atomic metal is increased, aggregation will inevitably occur. Therefore, a synthesis strategy that can achieve ultra-high single-atom loading and uniform distribution on the substrate needs to be designed.

(2) The development of HDACs is inseparable from the development and upgrading of characterization technology. In situ characterization techniques have made an indelible contribution to the exploration of atomic-scale catalysts, such as STEM, HRTEM, XAS, etc. However, these advanced devices are costly and scarce, limiting their universal use. With the progress of instrument science, more accurate observation magnitude and more convenient characterization methods need to be further developed.

(3) Let alone HDACs, the controllable synthesis of SACs has not been achieved so far. The coordination configurations of metal atoms are also not designable in the synthesis. Controlled synthesis methods that can construct target atomic-level configurations continue to be explored to obtain atomic-level catalysts with specific coordination configurations such as accurate coordination.

(4) For atomic-scale nano-catalytic drugs, the start and end of exogenously catalyzed reactions can be controlled by adjusting external stimuli, but endogenously catalyzed reactions are difficult to control. Excessive catalysis can lead to cellular oxidation and overexcitation, which can cause irreversible damage to healthy cells. For bimetallic atomic-scale catalysts, current anticancer treatments are carried out by endogenous trigger mechanisms. Therefore, the design of efficient HDACs for exogenous catalysis is the main direction in the future.

(5) Current application of DACs in the antitumor is mainly based on precious metals. However, it must be noted that in the field of nanomedical, even if a small number of active metal atoms can function, it will inevitably cause toxic damage to the liver and kidney. Therefore, the selection of metal elements with lower human cytotoxicity and even non-toxic non-metal single atoms (such as C, Si and P) to design HDACs will be more suitable for biomedical applications in the future.

(6) Clinical application has always been the ultimate goal of nanomedicine research. However, the successful application of DACs still requires consideration of many challenging issues, such as biocompatibility, pharmacokinetic properties, and immunogenicity. Therefore, the future design of HDACs should increase the proportion of practical application studies to facilitate clinical translation.

(7) Since the coordination structure and bonding state of bimetallic single atoms of HDACs are greatly affected by the surrounding environment, the relevant characterization techniques need to be further upgraded to observe the dynamic evolution process of the bimetallic sites to obtain more com-

prehensive and precise conclusions.

(8) Molecular targeted therapy with chemical agents is one of the first options for anti-tumor clinical treatment, but tumor cells frequently develop resistance to the drugs due to the following mechanisms that make the highly effective HDACs inactivated. (i) Autophagy in hunger response can be used to produce substances and energy necessary for tumor cell growth and has dual functions of non-protective and protective. Studies have found a 'switch' between the two functions of autophagy in tumor cells during drug administration, suggesting that protective autophagy of cells is one of the reasons for drug resistance. (ii) Mutations in certain genes such as epidermal growth factor receptor (EGFR) rare specific exon insertion mutation types will lead to binding site area of steric hindrance, hinder the effective combination of chemotherapy drugs, so that the sensitivity of tumor cells to chemotherapeutic drugs decreases. (iii) A number of studies have shown that overexpression of a variety of enzymes, including glutathione S-transferase (GST), is the main reason for inducing drug resistance. (iv) Abnormal signal pathway mediates drug resistance. For example, the nuclear transcription-related factor 2 (Nrf2)/antioxidant response element pathway (ARE) signaling pathway is one of the cellular defense mechanisms in the human body and phosphatidylinositol-3-kinase (PI3K)/protein kinase B (Akt) and extracellular signal-regulated kinase (MEK)/extracellular regulated protein kinase (ERK) signaling pathways are related to cell proliferation, differentiation, and apoptosis. (v) Some RNA regulate tumor cells to generate drug resistance. (vi) Related protein mediation leads to drug resistance. The appeal factors will seriously hinder the drug efficacy, and therefore it is urgent to develop novel HDAC drugs that can continue to maintain high activity.

At present, diatomic or polyatomic catalysts are mainly used in the field of electrocatalysis. It is expected that HDACs will exhibit a more amazing potential in the field of anti-tumor nanocatalytic medicine by further improving catalytic efficiency and enriching catalytic forms to make substantial progress and breakthroughs in the above aspects.

References

- [1] B. J. Sun, B. Lee, *Cancers*, **2022**, 14, 570.
- [2] P. Pei, T. Liu, W. Shen, Z. Liu, K. Yang, *Mater. Horiz.*, **2021**, 8, 1348–1366.
- [3] P. Schmid, J. Cortes, R. Dent, L. Pusztai, H. McArthur, S. Kummel, J. Bergh, C. Denkert, Y. H. Park, R. Hui, N. Harbeck, M. Takahashi, M. Untch, P. A. Fasching, F. Cardoso, J. Andersen, D. Patt, M. Danso, M. Ferreira, M. A. Mouret-Reynier, S. A. Im, J. H. Ahn, M. Gion, S. Baron-Hay, J. F. Boileau, Y. Ding, K. Tryfonidis, G. Aktan, V. Karantz, J. O'Shaughnessy, Keynotes-522. Investigators, *New Engl. J. Med.*, **2022**, 386, 556–567.
- [4] K. Kawahara, A. Hiraki, H. Arita, H. Takeshita, A. Hirose, Y. Matsuoka, J. Sakata, Y. Obayashi, H. Nakashima, M. Hirayama, M. Nagata, R. Yoshida, M. Shinohara, H. Nakayama, *Oral Dis.*, **2021**, 27, 1564–1571.
- [5] J. Han, J. Guan, *Nano Res.*, **2022**, 16, 1913–1966.
- [6] T. Tang, S. Li, J. Sun, Z. Wang, J. Guan, *Nano Res.*, **2022**, 15, 8714–8750.

- [7] X. Bai, Z. Duan, B. Nan, L. Wang, T. Tang, J. Guan, *Chin. J. Catal.*, **2022**, 43, 2240–2248.
- [8] X. Bai, J. Guan, *Chin. J. Catal.*, **2022**, 43, 2057–2090.
- [9] J. Han, M. Zhang, X. Bai, Z. Duan, T. Tang, J. Guan, *In org. Chem. Front.*, **2022**, 9, 3559–3565.
- [10] B. Jiang, Z. Guo, M. Liang, *Nano Res.*, **2023**, 16, 1878–1889.
- [11] M. Chang, Z. Hou, M. Wang, C. Li, A. A. Al Kheraif, J. Lin, *Chem. Eur. J.*, **2022**, 28, e202104081.
- [12] M. Li, H. Zhang, Y. Hou, X. Wang, C. Xue, W. Li, K. Cai, Y. Zhao, Z. Luo, *Nanoscale Horiz.*, **2020**, 5, 202–217.
- [13] T. Tang, Z. Wang, J. Guan, *Adv. Funct. Mater.*, **2022**, 32, 2111504.
- [14] N. Yang, W. Xiao, X. Song, W. Wang, X. Dong, *Nano-Micro Lett.*, **2020**, 12, 15.
- [15] J. Bonet-Aleta, J. I. Garcia-Peiro, J. L. Hueso, *Catalysts*, **2022**, 12, 167.
- [16] M. Zhao, R. Yang, Y. Wei, J. Su, X. Wang, N. Zhang, P. Sun, D. Chen, Y. Zhao, *Nano Today*, **2022**, 44, 101493.
- [17] Q. Liu, L. Shi, Y. Liao, X. Cao, X. Liu, Y. Yu, Z. Wang, X. Lu, J. Wang, *Adv. Sci.*, **2022**, 9, 2200005.
- [18] H. Lin, Y. Chen, J. Shi, *Chem. Soc. Rev.*, **2018**, 47, 1938–1958.
- [19] H. Pelicano, D. Carney, P. Huang, *Drug Resist. Updat.*, **2004**, 7, 97–110.
- [20] Q. Zhang, J. Guan, *Nano Res.*, **2021**, 15, 38–70.
- [21] Q. Zhang, J. Guan, *Energy Environ. Mater.*, **2020**, 4, 307–335.
- [22] K. Jiang, M. Luo, Z. Liu, M. Peng, D. Chen, Y. R. Lu, T. S. Chan, F. M. F. de Groot, Y. Tan, *Nat. Commun.*, **2021**, 12, 1687.
- [23] H. Xiong, A. K. Datye, Y. Wang, *Adv. Mater.*, **2021**, 33, 2004319.
- [24] Q. Zhang, J. Guan, *J. Power Sources*, **2020**, 471, 228446.
- [25] Z. L. Wang, J. Choi, M. Xu, X. Hao, H. Zhang, Z. Jiang, M. Zuo, J. Kim, W. Zhou, X. Meng, Q. Yu, Z. Sun, S. Wei, J. Ye, G. G. Wallace, D. L. Of-ficer, Y. Yamauchi, *ChemSusChem*, **2020**, 13, 929–937.
- [26] Z. X. Cai, Z. L. Wang, Y. J. Xia, H. Lim, W. Zhou, A. Taniguchi, M. Ohtani, K. Kobiro, T. Fujita, Y. Yamauchi, *Angew. Chem. Int. Ed.*, **2021**, 60, 4747–4755.
- [27] J. Han, J. Guan, *Chin. J. Catal.*, **2023**, 44, 1–3.
- [28] C.-C. Hou, H.-F. Wang, C. Lia, Q. Xu, *Energy Environ. Sci.*, **2020**, 13, 1658–1693.
- [29] C. Xiao, L. Cheng, Y. Zhu, G. Wang, L. Chen, Y. Wang, R. Chen, Y. Li, C. Li, *Angew. Chem. Int. Ed.*, **2022**, 61, e202206544.
- [30] L. Zhang, H. Bi, Z. Wang, G. Zhou, *Int. J. Hydrogen Energy*, **2022**, 47, 4653–4661.
- [31] M. Farnesi Camellone, F. Dvořák, M. Vorokhta, A. Tovt, I. Khalakhan, V. Johánek, T. Skála, I. Matolínová, S. Fabris, J. Mysliveček, *ACS Catal.*, **2022**, 12, 4859–4871.
- [32] S. Ji, Y. Chen, G. Zhao, Y. Wang, W. Sun, Z. Zhang, Y. Lu, D. Wang, *Appl. Catal. B*, **2022**, 304, 120922.
- [33] T. Zhu, Y. Han, S. Liu, B. Yuan, Y. Liu, H. Ma, *Front. Chem.*, **2021**, 9, 717201.
- [34] T. Tang, Z. Wang, J. Guan, *Acta Phys.-Chim. Sin.*, **2022**, 38, 2208033.
- [35] Y. Wang, R. Du, L. Y. S. Lee, K. Y. Wong, *Biosens. Bioelectron.*, **2022**, 216, 114662.
- [36] Z. Zhang, L. Bian, H. Tian, Y. Liu, Y. Bando, Y. Yamauchi, Z. L. Wang, *Small*, **2022**, 18, 2107450.
- [37] J. Tang, Y. Wu, X. Li, L. Bu, B. Chang, *Prog. Mater. Sci.*, **2022**, 128, 100959.
- [38] F. Meng, P. Zhu, L. Yang, L. Xia, H. Liu, *Chem. Eng. J.*, **2023**, 452, 139411.
- [39] J. Pei, H. Dou, C. Liu, T. Li, *J. Ind. Eng. Chem.*, **2022**, 109, 330–337.
- [40] F. Cao, Y. Sang, C. Liu, F. Bai, L. Zheng, J. Ren, X. Qu, *ACS Nano*, **2022**, 16, 855–868.
- [41] Y. Zhang, M. Chen, J. Wang, F. Cai, L. Ma, T. Chen, *Sci. China Chem.*, **2022**, 65, 1879–1884.
- [42] T. Tang, Z. Duan, D. Baimanov, X. Bai, X. Liu, L. Wang, Z. Wang, J. Guan, *Nano Res.*, **2023**, 16, 2218–2223.
- [43] F. Quan, G. Zhan, B. Zhou, C. Ling, X. Wang, W. Shen, J. Li, F. Jia, L. Zhang, *J. Environ. Sci.*, **2023**, 125, 544–552.
- [44] Y. Chen, J. Lin, B. Jia, X. Wang, S. Jiang, T. Ma, *Adv. Mater.*, **2022**, 34, 2201796.
- [45] Q. Zhang, J. Guan, *Solar RRL*, **2020**, 4, 2000283.
- [46] Q. Zhang, J. Guan, *Adv. Funct. Mater.*, **2020**, 30, 2000768.
- [47] T. Cai, Z. Teng, Y. Wen, H. Zhang, S. Wang, X. Fu, L. Song, M. Li, J. Lv, Q. Zeng, *J. Hazard. Mater.*, **2022**, 440, 129772.
- [48] S. Zhang, Y. Wu, Y.-X. Zhang, Z. Niu, *Sci. China Chem.*, **2021**, 64, 1908–1922.
- [49] X. Zheng, B. Li, Q. Wang, D. Wang, Y. Li, *Nano Res.*, **2022**, 15, 7806–7839.
- [50] J. Guan, *J. Power Sources*, **2021**, 506, 230143.
- [51] N. Liu, Q. Zhang, J. Guan, *Chem. Commun.*, **2021**, 57, 5016–5019.
- [52] J. Kari, J. P. Olsen, K. Jensen, S. F. Badino, K. B. R. M. Krogh, K. Borch, P. Westh, *ACS Catal.*, **2018**, 8, 11966–11972.
- [53] H. Ooka, J. Huang, K. S. Exner, *Front. Energy Res.*, **2021**, 9, 654460.
- [54] J.-L. Lin, I. Wheeldon, *ACS Catal.*, **2013**, 3, 560–564.
- [55] R. Li, D. Wang, *Adv. Energy Mater.*, **2022**, 12, 2103564.

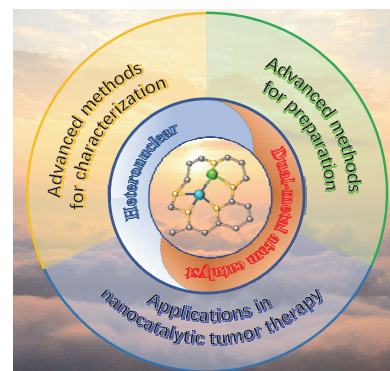
Graphical Abstract

Chin. J. Catal., 2023, 47: 1–31 doi: 10.1016/S1872-2067(22)64207-4

Heteronuclear dual-metal atom catalysts for nanocatalytic tumor therapy

Jingyi Han, Jingqi Guan*
Jilin University

In this review, we introduce how to construct and characterize heteronuclear dual-atom catalysts and emphatically discuss their application in the field of nanocatalytic tumor therapy.



- [56] C. Wang, K. Wang, Y. Feng, C. Li, X. Zhou, L. Gan, Y. Feng, H. Zhou, B. Zhang, X. Qu, H. Li, J. Li, A. Li, Y. Sun, S. Zhang, G. Yang, Y. Guo, S. Yang, T. Zhou, F. Dong, K. Zheng, L. Wang, J. Huang, Z. Zhang, X. Han, *Adv. Mater.*, **2021**, 33, 2003327.
- [57] L. Wu, T. Guo, T. Li, *Adv. Funct. Mater.*, **2022**, 32, 2203439.
- [58] R. Gusmão, M. Veselý, Z. Sofer, *ACS Catal.*, **2020**, 10, 9634–9648.
- [59] M. A. Bajada, J. Sanjose-Orduna, G. Di Liberto, S. Tosoni, G. Pacchioni, T. Noel, G. Vile, *Chem. Soc. Rev.*, **2022**, 51, 3898–3925.
- [60] J. Ge, D. Zhang, Y. Qin, T. Dou, M. Jiang, F. Zhang, X. Lei, *Appl. Catal. B*, **2021**, 298, 120557.
- [61] M. Liu, N. Li, S. Cao, X. Wang, X. Lu, L. Kong, Y. Xu, X. H. Bu, *Adv. Mater.*, **2022**, 34, 2107421.
- [62] D. Wu, B. He, Y. Wang, P. Lv, D. Ma, Y. Jia, *J. Phys. D*, **2022**, 55, 203001.
- [63] X. Lin, J. Zhang, J. Tang, Y. Yang, C. Liu, J. Huang, *Nanoscale*, **2022**, 14, 2482–2489.
- [64] C. B. Ma, Y. Xu, L. Wu, Q. Wang, J. J. Zheng, G. Ren, X. Wang, X. Gao, M. Zhou, M. Wang, H. Wei, *Angew. Chem. Int. Ed.*, **2022**, 61, e202116170.
- [65] L. Bai, C.-S. Hsu, D. T. L. Alexander, H. M. Chen, X. Hu, *Nat. Energy*, **2021**, 6, 1054–1066.
- [66] Z. W. Chen, L. X. Chen, C. C. Yang, Q. Jiang, *J. Mater. Chem. A*, **2019**, 7, 3492–3515.
- [67] J. Fu, J. Dong, R. Si, K. Sun, J. Zhang, M. Li, N. Yu, B. Zhang, M. G. Humphrey, Q. Fu, J. Huang, *ACS Catal.*, **2021**, 11, 1952–1961.
- [68] C. Liu, T. Li, X. Dai, J. Zhao, D. He, G. Li, B. Wang, X. Cui, *J. Am. Chem. Soc.*, **2022**, 144, 4913–4924.
- [69] L. Jiao, W. Ye, Y. Kang, Y. Zhang, W. Xu, Y. Wu, W. Gu, W. Song, Y. Xiong, C. Zhu, *Nano Res.*, **2021**, 15, 959–964.
- [70] S.-H. Kim, H. C. Song, S. J. Yoo, J. Han, K.-Y. Lee, H. C. Ham, *J. Mater. Chem. A*, **2022**, 10, 6216–6230.
- [71] Y. Wu, C. He, W. Zhang, *ACS Appl. Mater. Interfaces*, **2021**, 13, 47520–47529.
- [72] Y. Wu, C. He, W. Zhang, *J. Am. Chem. Soc.*, **2022**, 144, 9344–9353.
- [73] L. Bai, C. S. Hsu, D. T. L. Alexander, H. M. Chen, X. Hu, *J. Am. Chem. Soc.*, **2019**, 141, 14190–14199.
- [74] Y. Cao, C. Zhao, Q. Fang, X. Zhong, G. Zhuang, S. Deng, Z. Wei, Z. Yao, J. Wang, *J. Mater. Chem. A*, **2020**, 8, 2672–2683.
- [75] Y. Zhou, E. Song, W. Chen, C. U. Segre, J. Zhou, Y. C. Lin, C. Zhu, R. Ma, P. Liu, S. Chu, T. Thomas, M. Yang, Q. Liu, K. Suenaga, Z. Liu, J. Liu, J. Wang, *Adv. Mater.*, **2020**, 32, 2003484.
- [76] T. Tang, Y. Wang, J. Han, Q. Zhang, X. Bai, X. Niu, Z. Wang, J. Guan, *Chin. J. Catal.*, **2023**, 46, 48–55.
- [77] N. Yang, Y. Zhao, P. Wu, G. Liu, F. Sun, J. Ma, Z. Jiang, Y. Sun, G. Zeng, *Appl. Catal. B*, **2021**, 299, 120682.
- [78] R. Guo, M. Hu, W. Zhang, J. He, *Molecules*, **2019**, 24, 1777.
- [79] M. Xiao, H. Zhang, Y. Chen, J. Zhu, L. Gao, Z. Jin, J. Ge, Z. Jiang, S. Chen, C. Liu, W. Xing, *Nano Energy*, **2018**, 46, 396–403.
- [80] A. M. López Marzo, M. Guerrero, T. Calvet, M. Font-Bardia, E. Pellicer, M. D. Baró, J. Pons, J. Sort, *RSC Adv.*, **2015**, 5, 32369–32375.
- [81] E. Lee, S. H. Choi, H. C. Ham, *Nanoscale Adv.*, **2022**, 4, 2913–2921.
- [82] S. Feng, X. Lin, X. Song, Y. Liu, Z. Jiang, Y. Ding, *J. Catal.*, **2019**, 377, 400–408.
- [83] L. Jiao, L. Guo, *Catal. Lett.*, **2022**, DOI: 10.1007/s10562-022-04112-1.
- [84] X. Li, W. Zhong, P. Cui, J. Li, J. Jiang, *J. Phys. Chem. Lett.*, **2016**, 7, 1750–1755.
- [85] C. Wu, W. Yang, J. Wang, R. Kannaiyan, I. D. Gates, *Fuel*, **2021**, 305, 121547.
- [86] Y. Cao, J. Zhao, X. Zhong, G. Zhuang, S. Deng, Z. Wei, Z. Yao, J. Wang, *Green Energy Environ.*, **2021**, 6, 846–857.
- [87] C. N. Sun, Z. L. Wang, X. Y. Lang, Z. Wen, Q. Jiang, *ChemSusChem*, **2021**, 14, 4593–4600.
- [88] Y. Ying, X. Luo, J. Qiao, H. Huang, *Adv. Funct. Mater.*, **2020**, 31, 2007423.
- [89] H. Liu, Q. Huang, W. An, Y. Wang, Y. Men, S. Liu, *J. Energy Chem.*, **2021**, 61, 507–516.
- [90] Y. Zou, L. Wen, X. Bian, Y. Zhang, W. Lin, S. Huang, K. Ding, *Appl. Surf. Sci.*, **2021**, 569, 150921.
- [91] J. Wang, C. Liu, S. Li, Y. Li, Q. Zhang, Q. Peng, J. S. Tse, Z. Wu, *Chem. Eng. J.*, **2022**, 428, 132558.
- [92] Z. Zhang, X. Xu, *Adv. Theory Simul.*, **2022**, 5, 2100579.
- [93] X. Bai, L. Wang, B. Nan, T. Tang, X. Niu, J. Guan, *Nano Res.*, **2022**, 15, 6019–6025.
- [94] X. Wen, Q. Zhang, J. Guan, *Coord. Chem. Rev.*, **2020**, 409, 213214.
- [95] B. Yu, W. Wang, W. Sun, C. Jiang, L. Lu, *J. Am. Chem. Soc.*, **2021**, 143, 8855–8865.
- [96] X. Mao, Z. Deng, Y. Liu, H. Xie, Q. He, Y. Zhang, Z. Huang, H. Hu, T. Gan, *Appl. Surf. Sci.*, **2022**, 597, 153625.
- [97] X. Wei, C. Zhang, S. He, J. Huang, J. Huang, S. S. Liew, Z. Zeng, K. Pu, *Angew. Chem. Int. Ed.*, **2022**, 61, e202202966.
- [98] Z. Tang, P. Zhao, H. Wang, Y. Liu, W. Bu, *Chem. Rev.*, **2021**, 121, 1981–2019.
- [99] H. Jiang, Q. He, C. Wang, H. Liu, Y. Zhang, Y. Lin, X. Zheng, S. Chen, P. M. Ajayan, L. Song, *Adv. Energy Mater.*, **2018**, 8, 1800436.
- [100] H. Chen, Y. Zhang, Q. He, H. Zhang, S. Xu, X. He, H. Ji, *J. Mater. Chem. A*, **2020**, 8, 2364–2368.
- [101] O. Yadorao Bisen, A. Kumar Yadav, B. Pavithra, K. Kar Nanda, *Chem. Eng. J.*, **2022**, 449, 137705.
- [102] W. Shi, G. Xu, X. Han, Y. Wang, Z. Liu, S. Xue, N. Sun, X. Shi, Y. Yu, H. He, *J. Environ. Sci.*, **2023**, 126, 333–347.
- [103] S. Natori, M. Kurisu, N. Kawamura, Y. Takahashi, *Minerals*, **2022**, 12, 536.
- [104] N. Fernández-Delgado, M. Herrera, J. Pizarro, P. Galindo, S. I. Molina, *J. Mater. Sci.*, **2018**, 53, 15226–15236.
- [105] Z. Huang, H. Suzuki, M. Ito, S. Noguchi, *Int. J. Pharm.*, **2022**, 625, 122057.
- [106] G. Chupin, C. Tamain, T. Dumas, P. L. Solari, P. Moisy, D. Guillaumont, *Inorg. Chem.*, **2022**, 61, 4806–4817.
- [107] Y. Nishihata, O. Kamishima, Y. Kubozono, H. Maedab, S. Emurac, *J. Synchrotron Radiat.*, **1998**, 5, 1007–1009.
- [108] T. Egawa, M. Ito, S. Konaka, *J. Mol. Struct.*, **2001**, 560, 337–344.
- [109] N. Cefarin, D. E. Bedolla, A. Surowka, S. Donato, T. Sepperer, G. Tondi, D. Dreossi, N. Sodini, G. Birarda, L. Vaccari, *Int. J. Mol. Sci.*, **2021**, 22, 12869.
- [110] T. Petit, L. Puskar, *Diamond Relat. Mater.*, **2018**, 89, 52–66.
- [111] M. N. Filippov, V. P. Gavrilenko, M. V. Kovalchuk, V. B. Mityukhlyayev, Y. V. Ozerin, A. V. Rakov, V. V. Roddatis, P. A. Todua, A. L. Vasiliev, *Meas. Sci. Technol.*, **2011**, 22, 094014.
- [112] S. J. Haigh, H. Sawada, A. I. Kirkland, *Phys. Rev. Lett.*, **2009**, 103, 126101.
- [113] L. Crouzier, F. Pailloux, A. Delvallée, L. Devoille, N. Feltrin, C. Tromas, *Measurement*, **2021**, 180, 109521.
- [114] Joachim Loos, Erwan Sourty, S. V. Bavel, *Macromolecules*, **2009**, 42, 2581–2586.
- [115] Z. Wu, Y. Liu, X. Xing, L. Yao, Z. Chen, G. Mo, L. Zheng, Q. Cai, H. Wang, J. Zhong, Y. Lai, L. Qian, *Nano Res.*, **2022**, DOI: 10.1007/s12274-022-4742-3.
- [116] J. Guan, X. Bai, T. Tang, *Nano Res.*, **2021**, 15, 818–837.
- [117] X. Mou, D. Wang, X. Liu, W. Liu, L. Cao, T. Yao, *Radiat. Phys. Chem.*, **2020**, 175, 108230.
- [118] L. Fu, Y. Tang, Y. Lin, *Chem. Asian J.*, **2020**, 15, 2110–2116.
- [119] H. Yamashita, K. Yoshizawa, K. Kida, S. Ohshiro, M. Anpo, *Phys. Scr. T*, **2005**, 115, 691–694.

- [120] H. Funke, A.C. Scheinost, M. Chukalina, *Phys. Rev. B*, **2005**, 71, 094110.
- [121] J. Moon, M. Nilsson, *Dalton Trans.*, **2018**, 47, 15424–15438.
- [122] C. Asokan, L. DeRita, P. Christopher, *Chin. J. Catal.*, **2017**, 38, 1473–1480.
- [123] R. L. Mössbauer, *Z. Phys.*, **1958**, 15, 124–143.
- [124] C. Gallenkamp, U. I. Kramm, J. Proppe, V. Krewald, *Int. J. Quantum Chem.*, **2020**, 121, e26394.
- [125] J. Wang, Z. Huang, W. Liu, C. Chang, H. Tang, Z. Li, W. Chen, C. Jia, T. Yao, S. Wei, Y. Wu, Y. Li, *J. Am. Chem. Soc.*, **2017**, 139, 17281–17284.
- [126] G. Yang, J. Zhu, P. Yuan, Y. Hu, G. Qu, B. A. Lu, X. Xue, H. Yin, W. Cheng, J. Cheng, W. Xu, J. Li, J. Hu, S. Mu, J. N. Zhang, *Nat. Commun.*, **2021**, 12, 1734.
- [127] D. Bandyopadhyay, *Int. Mater. Rev.*, **2013**, 51, 171–208.
- [128] R. Senga, K. Suenaga, *Ultramicroscopy*, **2017**, 180, 150–155.
- [129] T. Akita, M. Okumura, K. Tanaka, S. Tsubota, *J. Electron Microsc.*, **2004**, 53, 29–35.
- [130] E. D. Boyes, P. L. Gai, *C. R. Phys.*, **2014**, 15, 200–213.
- [131] N. Tanaka, J. J. Hu, N. Baba, *Ultramicroscopy*, **199**, 78, 103–110.
- [132] G. E. Cutsail Iii, S. DeBeer, *ACS Catal.*, **2022**, 12, 5864–5886.
- [133] H. Stiel, J. Braenzel, A. Jonas, R. Gnewkow, L. T. Glogler, D. Sommer, T. Krist, A. Erko, J. Tummler, I. Mantouvalou, *Int. J. Mol. Sci.*, **2021**, 22, 13463.
- [134] Z. Xiao, Y. C. Huang, C. L. Dong, C. Xie, Z. Liu, S. Du, W. Chen, D. Yan, L. Tao, Z. Shu, G. Zhang, H. Duan, Y. Wang, Y. Zou, R. Chen, S. Wang, *J. Am. Chem. Soc.*, **2020**, 142, 12087–12095.
- [135] A. I. Protsenko, A. E. Blagov, Y. V. Pisarevsky, A. V. Rogachev, A. V. Targonsky, A. L. Trigub, I. A. Eliovich, S. N. Yakunin, M. V. Kovalchuk, *Phys.-Usp.*, **2021**, 64, 83–87.
- [136] Y. Mukai, M. Arahata, T. Tashima, R. Okamoto, S. Takeuchi, *Phys. Rev. Appl.*, **2021**, 15, 034019.
- [137] N. Analytical Methods Committee Amctb, *Anal. Methods*, **2021**, 13, 2997–3000.
- [138] L. Li, J. Wu, L. Yang, H. Wang, Y. Xu, K. Shen, *Cancer Manag. Res.*, **2021**, 13, 2389–2399.
- [139] T. Takaoka, M. Terahara, I. Kusunoki, *Surf. Sci.*, **2000**, 454–456, 218–221.
- [140] P. K. Huttunen, D. Labadini, S. S. Hafiz, S. Gokalp, E. P. Wolff, S. M. Martell, M. Foster, *Appl. Surf. Sci.*, **2021**, 554, 149518.
- [141] J. Wang, C. Z. Jin, X. Liu, D. R. Liu, H. Sun, F. F. Wei, T. Zhang, J. G. Stevens, A. Khasanov, I. Khasanova, *Hyperfine Interact.*, **2012**, 204, 111–117.
- [142] J. G. Stevens, J. C. Travis, J. R. Devoe, *Anal. Chem.*, **1972**, 44, 384–406.
- [143] J.-H. Hong, S.-J. Oh, S. J. Kwon, *Intermetallics*, **2003**, 11, 207–213.
- [144] V. V. Popov, *Phys. Met. Metallogr.*, **2012**, 113, 1257–1289.
- [145] V. S. Rusakov, K. K. Kadyrzhanov, *Hyperfine Interact.*, **2006**, 164, 87–97.
- [146] V. Mlynarik, *Anal. Biochem.*, **2017**, 529, 4–9.
- [147] B. Bechinger, C. Aisenbrey, P. Bertani, *Biochim. Biophys. Acta-Biomembr.*, **2004**, 1666, 190–204.
- [148] Z. Zhang, Y. Zhu, H. Asakura, B. Zhang, J. Zhang, M. Zhou, Y. Han, T. Tanaka, A. Wang, T. Zhang, N. Yan, *Nat. Commun.*, **2017**, 8, 16100.
- [149] H. B. Yang, S.-F. Hung, S. Liu, K. Yuan, S. Miao, L. Zhang, X. Huang, H.-Y. Wang, W. Cai, R. Chen, J. Gao, X. Yang, W. Chen, Y. Huang, H. M. Chen, C. M. Li, T. Zhang, B. Liu, *Nat. Energy*, **2018**, 3, 140–147.
- [150] L. Jiao, L. Guo, *Catal. Lett.*, **2022**, DOI: 10.1007/s10562-022-04106-z.
- [151] R. Hu, Y. Li, Q. Zeng, F. Wang, J. Shang, *ChemSusChem*, **2020**, 13, 3636–3644.
- [152] X. Wei, S. Cao, S. Wei, S. Liu, Z. Wang, F. Dai, X. Lu, *Appl. Surf. Sci.*, **2022**, 593, 153377.
- [153] Y. Li, *Green Energy Environ.*, **2020**, 5, 4–5.
- [154] S. K. Kaiser, A. H. Clark, L. Cartocci, F. Krumeich, J. Perez-Ramirez, *Small*, **2021**, 17, 2004599.
- [155] L. Peng, S. Yang, D. T. Sun, M. Asgari, W. L. Queen, *Chem. Commun.*, **2018**, 54, 10602–10605.
- [156] N. Cheng, X. Sun, *Chin. J. Catal.*, **2017**, 38, 1508–1514.
- [157] J. W. L. Eun, K. Seo, Hyung, M. Sung-Suh, M. M. Sung, *Chem. Mater.*, **2004**, 16, 1878–1883.
- [158] J. Fonseca, J. Lu, *ACS Catal.*, **2021**, 11, 7018–7059.
- [159] B. Shi, D. Shen, W. Li, G. Wang, *Macromol. Rapid Commun.*, **2022**, 43, 2200071.
- [160] X. Bai, Q. Sun, H. Cui, L. P. B. Guerzoni, S. Wuttke, F. Kiessling, L. De Laporte, T. Lammers, Y. Shi, *Adv. Mater.*, **2022**, 34, 2109701.
- [161] X. Wang, J. Sun, T. Li, Z. Song, D. Wu, B. Zhao, K. Xiang, W. Ai, X.-Z. Fu, J.-L. Luo, *Energy Stor. Mater.*, **2021**, 36, 409–416.
- [162] X. Wang, D. Wu, S. Liu, J. Zhang, X. Z. Fu, J. L. Luo, *Nano-Micro. Lett.*, **2021**, 13, 125.
- [163] E. Luo, Y. Chu, J. Liu, Z. Shi, S. Zhu, L. Gong, J. Ge, C.H. Choi, C. Liu, W. Xing, *Energy Environ. Sci.*, **2021**, 14, 2158–2185.
- [164] S. Swain, A. Altaee, M. Saxena, A. K. Samal, *Coord. Chem. Rev.*, **2022**, 470, 214710.
- [165] Q. Chen, P. Peng, G. Yang, Y. Li, M. Han, Y. Tan, C. Zhang, J. Chen, K. Jiang, L. Liu, C. Ye, E. Xing, *Angew. Chem. Int. Ed.*, **2022**, 61, e202205978.
- [166] J. Song, S. Liu, Y. Ji, W. Xu, J. Yu, B. Liu, W. Chen, J. Zhang, L. Jia, T. Zhu, Z. Zhong, G. Xu, F. Su, *Nano Res.*, **2022**, DOI: 10.1007/s12274-022-4790-8.
- [167] S. Ding, H.-A. Chen, O. Mekasuwandumrong, M. J. Hülsley, X. Fu, Q. He, J. Panpranot, C.-M. Yang, N. Yan, *Appl. Catal. B*, **2021**, 281, 119471.
- [168] V. Muravev, G. Spezzati, Y.-Q. Su, A. Parastaev, F.-K. Chiang, A. Longo, C. Escudero, N. Kosinov, E. J. M. Hensen, *Nat. Catal.*, **2021**, 4, 469–478.
- [169] J.-S. Jiang, H.-L. Wei, A.-D. Tan, R. Si, W.-D. Zhang, Y.-X. Yu, *Chin. J. Catal.*, **2021**, 42, 753–761.
- [170] D. Liu, K. Srinivas, X. Chen, F. Ma, X. Zhang, X. Wang, B. Wang, Y. Chen, *J. Colloid Interface Sci.*, **2022**, 624, 680–690.
- [171] J. Ma, L. Wang, Y. Deng, W. Zhang, T. Wu, Y. Song, *Sci. China Mater.*, **2020**, 64, 631–641.
- [172] Z. K. Yang, C.-Z. Yuan, A.-W. Xu, *ACS Energy Lett.*, **2018**, 3, 2383–2389.
- [173] S. Zhao, Y. Cheng, J.-P. Veder, B. Johannessen, M. Saunders, L. Zhang, C. Liu, M. F. Chisholm, R. De Marco, J. Liu, S.-Z. Yang, S. P. Jiang, *ACS Appl. Energy Mater.*, **2018**, 1, 5286–5297.
- [174] Y. Cao, F. Lei, Y. Li, S. Qiu, Y. Wang, W. Zhang, Z. Zhang, *J. Mater. Chem. A*, **2021**, 9, 16196–16207.
- [175] Q. Wang, T. Ina, W.-T. Chen, L. Shang, F. Sun, S. Wei, D. Sun-Waterhouse, S. G. Telfer, T. Zhang, G. I. N. Waterhouse, *Sci. Bull.*, **2020**, 65, 1743–1751.
- [176] K. Liu, B. Badamdorj, F. Yang, M. J. Janik, M. Antonietti, *Appl. Catal. B*, **2022**, 316, 121641.
- [177] S. Chen, M. Cui, Z. Yin, J. Xiong, L. Mi, Y. Li, *ChemSusChem*, **2021**, 14, 73–93.
- [178] Y. Ren, X. Wang, J. Ma, Q. Zheng, L. Wang, W. Jiang, *J. Mater. Sci. Technol.*, **2023**, 132, 223–251.
- [179] M. Feng, Y. Hu, P. Zhou, X. Wang, Y. He, X. Wang, D. Wang, *Chem. Eng. J.*, **2023**, 451, 138431.
- [180] L. Xiao, Z. Wang, J. Guan, *Coord. Chem. Rev.*, **2022**, 472, 214777.
- [181] T. Tang, Z. Wang, J. Guan, *Chin. J. Catal.*, **2022**, 43, 636–678.
- [182] H. Shen, T. Thomas, S. A. Rasaki, A. Saad, C. Hu, J. Wang, M. Yang,

- Electrochem. Energy Rev.*, **2019**, 2, 252–276.
- [183] S. Mallakpour, F. Sirous, C. M. Hussain, *Top. Curr. Chem.*, **2021**, 380, 7.
- [184] L. Jiao, G. Wan, R. Zhang, H. Zhou, S. H. Yu, H. L. Jiang, *Angew. Chem. Int. Ed.*, **2018**, 57, 8525–8529.
- [185] X. Yang, L. Yan, X. Kong, S. Liu, X. Zhao, *Adv. Sustainable Syst.*, **2021**, 6, 2100281.
- [186] S. Huang, Z. Qiao, P. Sun, K. Qiao, K. Pei, L. Yang, H. Xu, S. Wang, Y. Huang, Y. Yan, D. Cao, *Appl. Catal. B*, **2022**, 317, 121770.
- [187] J. Wang, W. Liu, G. Luo, Z. Li, C. Zhao, H. Zhang, M. Zhu, Q. Xu, X. Wang, C. Zhao, Y. Qu, Z. Yang, T. Yao, Y. Li, Y. Li, *Energy Environ. Sci.*, **2018**, 11, 3375–3379.
- [188] L. Zhang, J. Fischer, Y. Jia, X. Yan, W. Xu, X. Wang, J. Chen, D. Yang, H. Liu, L. Zhuang, M. Hankel, D. J. Searles, K. Huang, S. Feng, C. L. Brown, X. Yao, *J. Am. Chem. Soc.*, **2018**, 140, 10757–10763.
- [189] P. Xiao, X. Ge, H. Wang, Z. Liu, A. Fisher, X. Wang, *Adv. Funct. Mater.*, **2015**, 25, 1520–1526.
- [190] Z. Chen, G. Zhang, Q. Hu, Y. Zheng, S. Cao, G. Chen, C. Li, T. Boyko, N. Chen, W. Chen, T. Regier, J. Dynes, J. Wang, H.-T. Wang, J. Zhou, S. Sun, *Small Struct.*, **2022**, 3, 2200031.
- [191] S. Shen, Y. Sun, H. Sun, Y. Pang, S. Xia, T. Chen, S. Zheng, T. Yuan, *Catalysts*, **2022**, 12, 525.
- [192] H. Jing, Z. Zhao, J. Zhang, C. Zhu, W. Liu, N. Li, C. Hao, Y. Shi, D. Wang, *J. Phys. Chem. C*, **2021**, 125, 6147–6156.
- [193] J. Wang, G. Han, L. Wang, L. Du, G. Chen, Y. Gao, Y. Ma, C. Du, X. Cheng, P. Zuo, G. Yin, *Small*, **2018**, 14, 1704282.
- [194] J. Zhao, W. Yang, H. Yuan, X. Li, W. Bing, L. Han, K. Wu, *Catal. Lett.*, **2022**, DOI:10.1007/s10562-022-04016-0
- [195] H. Gao, J. Zang, X. Liu, Y. Wang, P. Tian, S. Zhou, S. Song, P. Chen, W. Li, *Appl. Surf. Sci.*, **2019**, 494, 101–110.
- [196] L. Tao, C.-Y. Lin, S. Dou, S. Feng, D. Chen, D. Liu, J. Huo, Z. Xia, S. Wang, *Nano Energy*, **2017**, 41, 417–425.
- [197] X. Sun, S. Sun, S. Gu, Z. Liang, J. Zhang, Y. Yang, Z. Deng, P. Wei, J. Peng, Y. Xu, C. Fang, Q. Li, J. Han, Z. Jiang, Y. Huang, *Nano Energy*, **2019**, 61, 245–250.
- [198] Z. Li, H. He, H. Cao, S. Sun, W. Diao, D. Gao, P. Lu, S. Zhang, Z. Guo, M. Li, R. Liu, D. Ren, C. Liu, Y. Zhang, Z. Yang, J. Jiang, G. Zhang, *Appl. Catal. B*, **2019**, 240, 112–121.
- [199] Z. Lu, B. Wang, Y. Hu, W. Liu, Y. Zhao, R. Yang, Z. Li, J. Luo, B. Chi, Z. Jiang, M. Li, S. Mu, S. Liao, J. Zhang, X. Sun, *Angew. Chem. Int. Ed.*, **2019**, 58, 2622–2626.
- [200] D. Liu, B. Wang, H. Li, S. Huang, M. Liu, J. Wang, Q. Wang, J. Zhang, Y. Zhao, *Nano Energy*, **2019**, 58, 277–283.
- [201] P. Zhou, X. Hou, Y. Chao, W. Yang, W. Zhang, Z. Mu, J. Lai, F. Lv, K. Yang, Y. Liu, J. Li, J. Ma, J. Luo, S. Guo, *Chem. Sci.*, **2019**, 10, 5898–5905.
- [202] W. Liu, H. Zhang, C. Li, X. Wang, J. Liu, X. Zhang, *J. Energy Chem.*, **2020**, 47, 333–345.
- [203] S. Tian, B. Wang, W. Gong, Z. He, Q. Xu, W. Chen, Q. Zhang, Y. Zhu, J. Yang, Q. Fu, C. Chen, Y. Bu, L. Gu, X. Sun, H. Zhao, D. Wang, Y. Li, *Nat. Commun.*, **2021**, 12, 3181.
- [204] A. Shan, X. Teng, Y. Zhang, P. Zhang, Y. Xu, C. Liu, H. Li, H. Ye, R. Wang, *Nano Energy*, **2022**, 94, 106913.
- [205] A. Aijaz, A. Karkamkar, Y. J. Choi, N. Tsumori, E. Ronnebro, T. Autrey, H. Shioyama, Q. Xu, *J. Am. Chem. Soc.*, **2012**, 134, 13926–13929.
- [206] Y. Chen, S. Ji, C. Chen, Q. Peng, D. Wang, Y. Li, *Joule*, **2018**, 2, 1242–1264.
- [207] J. Wang, R. You, C. Zhao, W. Zhang, W. Liu, X.-P. Fu, Y. Li, F. Zhou, X. Zheng, Q. Xu, T. Yao, C.-J. Jia, Y.-G. Wang, W. Huang, Y. Wu, *ACS Catal.*, **2020**, 10, 2754–2761.
- [208] M. Xiao, J. Zhu, S. Li, G. Li, W. Liu, Y.-P. Deng, Z. Bai, L. Ma, M. Feng, T. Wu, D. Su, J. Lu, A. Yu, Z. Chen, *ACS Catal.*, **2021**, 11, 8837–8846.
- [209] X. Zhu, D. Zhang, C.-J. Chen, Q. Zhang, R.-S. Liu, Z. Xia, L. Dai, R. Amal, X. Lu, *Nano Energy*, **2020**, 71, 104597.
- [210] P. E. Imoisili, J. Ren, T.-C. Jen, *Electrochem. Commun.*, **2022**, 135, 107215.
- [211] S. Zhang, B. Zhang, Z. Li, X. Yang, F. Meng, H. Liang, Y. Lei, H. Wu, J. Zhang, G. Li, Y. Qin, *Cell Rep. Phys. Sci.*, **2022**, 3, 100787.
- [212] J. Lu, *Acc. Mater. Res.*, **2022**, 3, 358–368.
- [213] J. Plutnar, M. Pumera, *Small*, **2021**, 17, 2102088.
- [214] Y. Yang, Y. Zhang, L. Bai, D. M. Malouangou, J. T. Matondo, J. Pan, S. Dai, M. Cai, X. Liu, M. Guli, *J. Mater. Chem. C*, **2022**, 10, 819–839.
- [215] J. Fu, S. Wang, Z. Wang, K. Liu, H. Li, H. Liu, J. Hu, X. Xu, H. Li, M. Liu, *Front. Phys.*, **2020**, 15, 33201.
- [216] H. Yan, Y. Lin, H. Wu, W. Zhang, Z. Sun, H. Cheng, W. Liu, C. Wang, J. Li, X. Huang, T. Yao, J. Yang, S. Wei, J. Lu, *Nat. Commun.*, **2017**, 8, 1070.
- [217] L. Zhang, R. Si, H. Liu, N. Chen, Q. Wang, K. Adair, Z. Wang, J. Chen, Z. Song, J. Li, M. N. Banis, R. Li, T. K. Sham, M. Gu, L. M. Liu, G. A. Botton, X. Sun, *Nat. Commun.*, **2019**, 10, 4936.
- [218] L. Zhang, H. Liu, S. Liu, M. Norouzi Banis, Z. Song, J. Li, L. Yang, M. Markiewicz, Y. Zhao, R. Li, M. Zheng, S. Ye, Z.-J. Zhao, G. A. Botton, X. Sun, *ACS Catal.*, **2019**, 9, 9350–9358.
- [219] B. P. Le Monnier, L. Savereide, M. Kılıç, R. Schnyder, M. D. Mensi, C. E. Avalos, U. Rothlisberger, J. S. Luterbacher, *ACS Sustainable Chem. Eng.*, **2022**, 10, 3455–3465.
- [220] L. Deng, S. Han, Y. Li, W. Shen, *ChemCatChem*, **2022**, 14, e202200400.
- [221] Y. Wu, C. Ye, L. Yu, Y. Liu, J. Huang, J. Bi, L. Xue, J. Sun, J. Yang, W. Zhang, X. Wang, P. Xiong, J. Zhu, *Energy Storage Mater.*, **2022**, 45, 805–813.
- [222] R. Zhan, Y. Zhou, C. Liu, X. Wang, X. Sun, Y. Zhu, J. Niu, *Sep. Purif. Technol.*, **2022**, 286, 120443.
- [223] Z. Cao, D. Li, J. Wang, X. Yang, *Acta Biomater.*, **2021**, 130, 17–31.
- [224] S. Aldosari, M. Awad, E. O. Harrington, F. W. Sellke, M. R. Abid, *Antioxidants*, **2018**, 7, 14.
- [225] C. Zhang, X. Wang, J. Du, Z. Gu, Y. Zhao, *Adv. Sci.*, **2021**, 8, 2002797.
- [226] M. F. Huang, W. L. Lin, Y. C. Ma, *Indoor Air*, **2005**, 15, 135–140.
- [227] O. Warburg, *Science*, **1956**, 123, 309–314.
- [228] Z. Yu, Y. Hu, Y. Sun, T. Sun, *Chem. Eur. J.*, **2021**, 27, 13953–13960.
- [229] Y. Liu, M. Yao, W. Han, H. Zhang, S. Zhang, *Chem. Eur. J.*, **2021**, 27, 13418–13425.
- [230] Y. Zhuang, S. Han, Y. Fang, H. Huang, J. Wu, *Coord. Chem. Rev.*, **2022**, 455, 214360.
- [231] Y. Yin, L. Shi, W. Li, X. Li, H. Wu, Z. Ao, W. Tian, S. Liu, S. Wang, H. Sun, *Environ. Sci. Technol.*, **2019**, 53, 11391–11400.
- [232] X. Du, S. Wang, F. Ye, Z. Qingrui, *Environ. Res.*, **2022**, 206, 112414.
- [233] Y. Jiang, J. Ran, K. Mao, X. Yang, L. Zhong, C. Yang, X. Feng, H. Zhang, *Ecotoxicol. Environ. Saf.*, **2022**, 236, 113464.
- [234] S. Ziembowicz, M. Kida, *Chemosphere*, **2022**, 296, 134041.
- [235] J. Yang, H. Yao, Y. Guo, B. Yang, J. Shi, *Angew. Chem. Int. Ed.*, **2022**, 61, e202200480.
- [236] S. Wang, Z. Hu, Q. Wei, P. Cui, H. Zhang, W. Tang, Y. Sun, H. Duan, Z. Dai, Q. Liu, X. Zheng, *ACS Appl. Mater. Interfaces*, **2022**, 14, 20669–20681.
- [237] M. Zhang, D. Yang, C. Dong, H. Huang, G. Feng, Q. Chen, Y. Zheng, H. Tang, Y. Chen, X. Jing, *ACS Nano*, **2022**, 16, 9938–9952.
- [238] X. Wang, X. Wang, X. Zhong, G. Li, Z. Yang, Y. Gong, Z. Liu, L. Cheng, *Appl. Phys. Rev.*, **2020**, 7, 041411.
- [239] J. Liu, S. Fu, J. Xie, J. Zhang, J. Pan, C. Chu, G. Liu, S. Ju, *Biosensors*,

- 2022, 12, 255.
- [240] Y. Yu, L. Tan, Z. Li, X. Liu, Y. Zheng, X. Feng, Y. Liang, Z. Cui, S. Zhu, S. Wu, *ACS Nano*, **2021**, 15, 10628–10639.
- [241] X. Feng, J. Lei, L. Ma, Q. Ouyang, Y. Zeng, H. Liang, C. Lei, G. Li, L. Tan, X. Liu, C. Yang, *Small*, **2022**, 18, 2105775.
- [242] C. Zhang, C. Xu, X. Gao, Q. Yao, *Theranostics*, **2022**, 12, 2115–2132.
- [243] A. M. Florea, D. Busselberg, *Cancers*, **2011**, 3, 1351–1371.
- [244] C. S. Allardyce, P. J. Dyson, D. J. Ellis, S. L. Heath, *Chem. Commun.*, **2001**, 1396–1397.
- [245] N. Kordestani, E. Abas, L. Grasa, A. Alguacil, F. Scalambra, A. Romerosa, *Chem. Eur. J.*, **2022**, 28, e202103048.

用于纳米催化肿瘤治疗的异核双金属原子催化剂

韩璟怡, 管景奇*

吉林大学化学学院物理化学研究所, 吉林长春130021

摘要: 癌症是威胁人类健康的重大疾病之一。目前, 化疗、放疗和手术治疗是三大常规治疗癌症手段, 虽然这些治疗技术成熟, 但都存在不足, 且治疗成本高昂, 并使得患者在治疗过程中承受痛苦。因此, 开发活性位点丰富、催化效率高、肿瘤组织识别准确的新型抗肿瘤催化材料, 利用有限的治疗资源, 以最低的毒性取得最佳的治疗效果, 成为癌症治疗的研究新前沿。随着纳米材料的快速发展, 异核双原子催化剂(HDACs)在保留单原子催化剂的最大原子利用率, 活性位点分布均匀, 孤立单原子的不饱和配位环境和有利于电荷转移的电子结构等优点的基础上, 其两种不同金属原子不仅能提供更丰富的反应活性位点, 两者之间还具有独特的协同作用, 可以有效突破单原子催化剂的线性限制并优化活性中间物种的吸附能垒和构型, 显著提高催化活性和选择性从而获得满意的治疗效果, 在纳米催化肿瘤治疗领域展现出巨大的实际应用潜力。

本文对HDACs的表征手段、制备方法及其近年来在纳米催化肿瘤治疗领域的应用进行了系统的综述。首先简要介绍了原子水平活性位点的各种表征方法, 特别是原位技术, 讨论了它们应用的侧重点, 并比较了各自的优缺点。其次, 由于反应原子的高表面自由能、难以调控的动力学行为以及与载体的弱结合使得HDACs在合成过程中极不稳定。一旦异质活性金属原子之间的距离变近, 就不可避免地发生团聚, 从而形成合金或大尺寸的纳米颗粒。因此, 实现HDACs的精确和可控合成一直是该领域的研究重点。本文对HDACs的四大主要制备策略即传统的高温热解法、湿式化学双溶剂法、原子层沉积技术和软模板自组装技术进行了系统总结, 并简要介绍了相关催化剂的应用潜力。再次, 概括性地阐明了HDACs的抗肿瘤治疗机理, 并依据其发挥疗效的机理, 针对性地将近年来应用于抗癌领域的HDACs划分为芬顿/类芬顿反应或其他机制两大类, 并对这两类HDACs进行了详细的介绍。最后, 探讨了HDACs在抗肿瘤领域可能面临的问题和挑战并展望了未来研究方向和应用前景, 以期应用于该领域HDACs的研究提供富有价值的借鉴。

关键词: 异核; 双原子催化剂; 肿瘤治疗; 活性氧; 类芬顿反应

收稿日期: 2022-10-30. 接受日期: 2022-12-01. 上网时间: 2023-03-20.

*通讯联系人. 电子信箱: guanjq@jlu.edu.cn (管景奇).

基金来源: 国家自然科学基金(22075099); 吉林省自然科学基金项目(20220101051Jc); 吉林省教育厅(JJKH20220967KJ).